

Future Evolution of Bound Superclusters in an Accelerating Universe

Pablo A. Araya-Melo¹, Andreas Reisenegger², Andrés Meza³, Rien van de Weygaert¹, Rolando Dünner², and Hernán Quintana²

¹*Kapteyn Astronomical Institute, University of Groningen, P.O. Box 800, 9700 AV Groningen, The Netherlands*

²*Departamento de Astronomía y Astrofísica, Facultad de Física, P. Universidad Católica de Chile, Casilla 306, Santiago 22, Chile*

³*Departamento de Ciencias Físicas, Facultad de Ingeniería, Universidad Andres Bello, Santiago, Chile*

10 November 2018

ABSTRACT

The evolution of marginally bound supercluster-like objects in an accelerating Universe, with a cosmological constant $\Omega_{\Lambda,0} = 0.7$ and $\Omega_{m,0} = 0.3$, is followed from the present time to an expansion factor $a = 100$. The large scale evolution of these objects freezes shortly after the present cosmological epoch, in contrast to the vigorously continuing internal development. Our study follows the external and the internal evolution of these *island universes*, as they gradually detach themselves from the cosmic background and internally evolve in splendid isolation. We model the bound objects in a large Λ CDM cosmological simulation of 512^3 dark matter particles in a cube of $500h^{-1}\text{Mpc}$ side length. The objects are identified on the basis of the binding density criterion introduced by Dünner et al. (2006). Superclusters are identified with the ones whose mass $M > 10^{15}h^{-1}M_{\odot}$. In our simulation we find one supercluster with a mass of $M \sim 8 \times 10^{15}h^{-1}M_{\odot}$, slightly larger than that of the Shapley supercluster. Even though we find around two Shapley-like superclusters in a volume comparable to that of the Local Universe ($z < 0.1$), these massive superclusters do contain less clusters than the Shapley or Horologium-Reticulum concentrations. We construct the supercluster, bound object and virialized halo mass functions at $a = 1$ and at $a = 100$. As a manifestation of the large-scale evolution, we find them to hardly change after the present epoch. Using the linearly extrapolated binding overdensity as critical density value, the corresponding Press-Schechter and Sheth-Tormen mass functions do succeed in reproducing the simulation mass function of bound objects. The Jenkins mass function gives the best description of the virialized halos, but fails in the case of the superclusters and bound objects. Three manifestations of the internal evolution have been explored. These are the shape of the bound objects, their compactness and density profile, and the substructure of the superclusters in terms of their multiplicity function. While most superclusters are prolate at $a = 1$, we find them to evolve towards a nearly spherical shape at $a = 100$. We also find that they become highly concentrated, with near isothermal density profiles. Meanwhile their substructure disappears towards the far future, as their substructure and subclumps fall in and merge to form one coherent virialized system.

Key words: Cosmology: theory – large-scale structure of Universe – galaxies: clusters: general

1 INTRODUCTION

The evidence for an accelerated expansion of the Universe has established the possibility of a ‘dark energy’ component. In this scenario, the universe is entering into an accelerating phase, which is increasingly dominated by the dark energy. It is assumed that this dark energy, in its simplest form, behaves like Einstein’s cosmological constant.

As long as the matter density in the universe dominated over that of dark energy, gravitational structure formation resulted in the emergence of ever larger structures. Once dark energy came to dominate and the universe got into accelerated expansion, structure formation came to a halt (Peebles 1980; Heath 1977). With the present-day universe having reached this stage, the largest identifiable objects that will ever populate our universe may be the ones that

we observe in the process of formation at the present cosmological time. While no larger objects will emerge, these sufficiently overdense and bound patches will not be much affected by the global cosmic acceleration. They will remain bound and evolve as if they are *island universes*: they turn into isolated evolving regions (Chiueh & He 2002; Nagamine & Loeb 2003; Busha et al. 2003; Dünner et al. 2006).

While clusters of galaxies are the most massive and most recently fully collapsed and virialized structures, the present day superclusters are arguably the largest bound but not yet fully evolved objects in our Universe. In our accelerating universe we may assume they are the objects that ultimately will turn into island universes. A large range of observational studies, mostly based on optically or X-ray selected samples, show that clusters are strongly clustered and group together in large supercluster complexes (see e.g. Oort 1983; Bahcall 1988; Einasto et al. 1994, 2001; Quintana et al. 2000). These superclusters, the largest structures identifiable in the present Universe, are enormous structures comprising a few up to dozens of rich clusters of galaxies, a large number of more modestly sized clumps and thousands of galaxies spread between these density concentrations.

In this study we aim at contrasting the large scale evolution of structure in an accelerated Universe with that of the internal evolution of bound objects. In order to infer what will be the largest bound regions in our Universe, the *island universes*, we study the mass function of bound objects. The abundance or mass function of superclusters serves as a good indicator of the growth of structure of a cosmological model. While large scale structure formation comes to a halt this will manifest itself in the asymptotic behaviour of the supercluster mass function. Meanwhile, the internal evolution of the superclusters continues as they contract and collapse into the largest virialized entities the universe will ever contain.

We address three aspects of the continuing internal evolution of bound regions: their shape, density profile and internal substructure in terms of their cluster multiplicity. The shape of supercluster regions is one of the most sensitive probes of their evolutionary stage. We know that superclusters in the present-day Universe are mostly flattened or elongated structures, usually identified with the most prominent filaments and sheets in the galaxy distribution (e.g. Plionis et al. 1992; Sathyaprakash et al. 1998; Basilakos et al. 2001; Sheth, Sahni, Shandarin 2003; Einasto et al. 2007). The Pisces-Perseus supercluster chain is a particularly well-known example of a strongly elongated filament (see e.g. Haynes et al. 1986). The distribution of shapes of bound structures is a combination of at least two factors. One is the shape of the proto-supercluster in the initial density field. The second factor is the evolutionary state of the bound structure. We know that the gravitational collapse of cosmic overdensities — whose progenitors in the primordial density perturbation field will never be spherical (Bardeen et al. 1986; Peacock & Heavens 1985) — proceeds in a distinctly anisotropic fashion via flattened and elongated configurations towards a final more compact triaxial virialized state (see eg. Zeldovich 1970; Icke 1973; White & Silk 1979; Eisenstein & Loeb 1995;

Bond & Myers 1996; Sathyaprakash et al. 1996; Desjacques 2008; van de Weygaert & Bond 2008).

The collapse of the superclusters will also result in a continuous sharpening of the internal mass distribution, reflected in their density profile. While they are still in the process of full collapse one may still recognize the internal substructure of its constituent clusters. As its subclumps merge into ever more massive concentrations, the mass distribution will attain a more uniform character. We therefore also study their evolving and decreasing level of substructure. We follow the evolving supercluster multiplicity function, i.e. the number of cluster-sized clumps within the realm of the bound supercluster region.

Representing moderate density enhancements on scale of tens of Mpc, in the present Universe superclusters are still expanding with the Hubble flow, although at a slightly decelerated rate, or have just started contracting. Because these structures have not yet fully formed, virialized and clearly separated from each other, it is difficult to identify them unambiguously. In most studies superclusters have been defined by more or less arbitrary criteria, mostly on the basis of a grouping and/or percolation algorithm (see e.g. Oort 1983; Bahcall 1988; Einasto et al. 1994, 2001; Quintana et al. 2000). This introduces the need for a user-specified percolation radius. Dünner et al. (2006, hereafter Paper I) attempted to define a more physically based criterion, identifying superclusters with the biggest gravitationally bound structures that will be able to form in our Universe. On the basis of this, they worked out a lower density limit for gravitationally bound structures. This limit is based on the density contrast that a spherical shell needs to attain to remain bound to a spherically symmetric overdensity.

We use this spherical density criterion to identify bound structures in a large cosmological box. In this we follow the work of Chiueh & He (2002) and Dünner et al. (2006). Chiueh & He (2002) numerically solved the spherical collapse model equations for self-consistent growing mode perturbations in order to obtain a theoretical criterion for the mean density enclosed in the outer gravitationally bound shell. The resulting density criterion was evaluated by Dünner et al. (2006) on the basis of numerical simulations. They generalized it by deriving the analytical solution which also forms the basis of the current study, and in Dünner et al. (2007) extended the criterion to limits for bound structures in redshift space.

Various authors have addressed the future evolution of cosmic structure (Chiueh & He 2002; Busha et al. 2003; Nagamine & Loeb 2003; Dünner et al. 2006, 2007; Hoffman et al. 2007; Busha et al. 2007). The internal evolution of the density and velocity structures of bound objects was followed by Busha et al. (2003), with Busha et al. (2007) focusing on the effects of small-scale structure on the formation of dark matter halos in two different cosmologies. Nagamine & Loeb (2003) specifically focused on the evolution of the Local Universe, which got extended by Hoffman et al. (2007) towards an investigation of the dependence on dark matter and dark energy. Nagamine & Loeb (2003) found that the Local Group will get detached from the rest of the Universe, and that its physical distance to other systems will increase exponentially. A key point of attention in Nagamine & Loeb (2003), Hoffman et al. (2007) and Busha et al. (2007) was the mass function of objects in

their simulations, on which they all agree in that it hardly changes after the current cosmic epoch.

This paper is organized as follows. In section 2, we present a review of the spherical collapse model and a prescription for deriving an analytical solution for the spherical collapse equations. Section 3 describes the simulation and the group finder algorithm that we employ when determining the mass functions. Section 4 presents the mass functions of the bound structures at $a = 1$ and $a = 100$ and a comparison with the ones obtained by the Press-Schechter formalism and its variants. Shapes of the structures are studied in section 5. In section 6 we look into the mass distribution and density profiles. Section 7 presents the study of the supercluster multiplicity function. Its results are taken along in sect. 8 with those on the supercluster mass functions we obtained in section 4 to relate our findings to the presence and abundance of monster supercluster complexes like the Shapley and Horologium-Reticulum supercluster. Finally, in section 9, we discuss our findings and draw conclusions on various issues addressed by our study.

2 SUPERCLUSTER COLLAPSE MODEL

The present study is based on an attempt towards a more physical criterion for the definition of superclusters, specifically the one proposed by Dünner et al. (2006). One could imagine a variety of physical definitions for superclusters, mostly relating to the assumption that they are the largest bound structures in the Universe, just having commenced to condense out of the cosmic background. One particular criterion would be to invoke the corresponding velocity field and identify them with bound regions that have turned around and started to contract, on the way towards complete collapse and virialization. In practice it would be more straightforward to try to relate an (approximate) density threshold to regions that are gravitationally bound. Given the anisotropic nature of the collapse and the tidal influence of the cosmic surroundings (Zeldovich 1970; Icke 1973; Bond & Myers 1996; Sheth & Tormen 1999; Desjacques 2008; van de Weygaert & Bond 2008) this may only yield a rough approximation. The work by Sheth & Tormen (1999) did show that a density threshold does depend on shape and environment. Nonetheless, we assume that a global density threshold criterion, in combination with a few extra assumptions, does assure a reasonably accurate identification process. This has indeed been demonstrated by Dünner et al. (2006) in a comparison of the criterion with the outcome of numerical simulations.

Dünner et al. (2006) derived an analytical criterion for a density threshold criterion for bound regions in a universe with dark energy. We summarize this criterion and derivation in the subsections below. In addition to the density threshold, we assure that a given bound region has started to materialize as a recognizable entity by including the additional requirement of the bound regions to have a virialized core. In a final step we group the overlapping identified spherical bound supercluster objects in order to outline a region that in the observational reality would be recognized as a supercluster.

The spherical density criterion described below forms a key ingredient of our supercluster definition and for the iden-

tification procedure for singling out bound spherical regions associated with clusters (sect. 3.1.4).

2.1 Spherical Collapse Model

The spherical collapse model (Gunn & Gott 1972; Lilje & Lahav 1991; Lahav et al. 1991) describes the evolution of a spherically symmetric mass density perturbation in an expanding Universe. Its great virtue is the ability to completely follow the nonlinear evolution of a collapsing shell, as the dynamics is fully and solely determined by the (constant) mass interior to the shell. Even though the gravitational collapse of generic cosmological structures tends to be highly inhomogeneous and anisotropic, the spherical model has proven to provide a surprisingly accurate description of the more complex reality. Even in situations where it is not able to provide accurate quantitative predictions it may be used as a good reference for interpretation of results.

Because of the key importance of the spherical collapse model for our bound object and supercluster identification procedure, we here present a short description following the formalism by Dünner et al. (2006). For a detailed and complete derivation we refer to this publication.

We consider a flat FRW Universe with a cosmological constant Λ . The mass density parameter at the current epoch is $\Omega_{m,0}$, while $\Omega_{\Lambda,0}$ is the present value of the cosmological density parameter. The Hubble parameter at the current epoch is H_0 .

A mass shell with a (physical) radius $r(t)$ at time t encloses a fixed mass M . The starting point of our derivation is the energy E per unit mass of the shell, which satisfies the equation (Peebles 1984):

$$E = \frac{1}{2} \left(\frac{dr}{dt} \right)^2 - \frac{GM}{r} - \frac{\Lambda r^2}{6} = \text{constant}, \quad (1)$$

By introducing the dimensionless variables

$$\tilde{r} = \left(\frac{\Lambda}{3GM} \right)^{\frac{1}{3}} r, \quad (2)$$

$$\tilde{t} = \left(\frac{\Lambda}{3} \right)^{\frac{1}{2}} t, \quad (3)$$

$$\tilde{E} = \left(\frac{G^2 M^2 \Lambda}{3} \right)^{-\frac{1}{2}} E. \quad (4)$$

the energy equation can be recast into the simpler dimensionless form

$$\tilde{E} = \frac{1}{2} \left(\frac{d\tilde{r}}{d\tilde{t}} \right)^2 - \frac{1}{\tilde{r}} - \frac{\tilde{r}^2}{2}. \quad (5)$$

2.2 Critical shell and turnaround radius

To delineate a bound regions around a spherical mass concentration we have to identify the critical shell. It is the shell that asymptotically separates the regions that will expand forever and the ones that will at some moment in time turn around and fall in onto the core of the region.

In a Universe with a cosmological constant, the critical shell is the one that delimits the region of gravitational attraction and the region of repulsion. This translates it-

self into the radius for which the (dimensionless) potential energy \tilde{V} is maximized,

$$\tilde{V} = -\frac{1}{\tilde{r}} - \frac{\tilde{r}^2}{2} \quad (6)$$

The maximum of this potential occurs at $\tilde{r}^* = 1$. In other words, the maximum possible energy for a shell to remain attached to the spherical mass concentration is

$$\tilde{E}^* = \tilde{V}(\tilde{r}^* = 1) = -\frac{3}{2} \quad (7)$$

Note that the maximum radius \tilde{r}_{\max} of the critical shell is reached when $V(\tilde{r}_{\max}) = \tilde{E}^* = -\frac{3}{2}$, i.e. when

$$r_{\max} = \left(\frac{3GM}{\Lambda} \right)^{1/3}, \quad (8)$$

so that the normalized radius can be interpreted as $\tilde{r} = r/r_{\max}$.

2.3 Connection Background Universe

Assuming a flat Universe with cosmological constant, the age of the Universe may be related to the vacuum energy density parameter (Peebles 1980)

$$\Omega_{\Lambda}(\tilde{t}) \equiv \frac{\Lambda}{3H^2} = \tanh^2 \left(\frac{3\tilde{t}}{2} \right), \quad (9)$$

showing that Ω_{Λ} increases monotonically in time.

In order to find the value of the radius of the critical shell, \tilde{r}_{cs} (we use the subscript 'cs' to indicate we are referring to a critical shell), as a function of Ω_{Λ} we need to invoke the solution of the shell radius \tilde{r}_{cs} as a function of cosmic time \tilde{t} .

In the particular case of a critical shell, for which $\tilde{E} = \tilde{E}^* = \frac{3}{2}$, one may infer the expression for \tilde{r}_{cs} by integrating the energy equation (5) from $\tilde{t} = 0$ ($\tilde{r} = 0$) until epoch \tilde{t} ($\tilde{r}(t) = \tilde{r}$),

$$\tilde{t} = \int_0^{\tilde{r}} \frac{\sqrt{r} dr}{(1-r)\sqrt{r+2}}. \quad (10)$$

The integral can be evaluated analytically, yielding the solution

$$\tilde{t} = \frac{1}{2\sqrt{3}} \ln \left(\frac{1+2\tilde{r} + \sqrt{3\tilde{r}(\tilde{r}+2)}}{1+2\tilde{r} - \sqrt{3\tilde{r}(\tilde{r}+2)}} \right) - \ln(1+\tilde{r} + \sqrt{\tilde{r}(\tilde{r}+2)}). \quad (11)$$

Substituting eqn. (11) in the expression for Ω_{Λ} (eqn. 9), and introducing the variable

$$\chi(\tilde{r}) = \left[\frac{1+2\tilde{r} + \sqrt{3\tilde{r}(\tilde{r}+2)}}{1+2\tilde{r} - \sqrt{3\tilde{r}(\tilde{r}+2)}} \right]^{\frac{\sqrt{3}}{2}} \times (1+\tilde{r} + \sqrt{\tilde{r}(\tilde{r}+2)})^{-3}, \quad (12)$$

we find that the value of Ω_{Λ} at the time when the critical shell has radius \tilde{r} is given by

$$\Omega_{\Lambda}(\tilde{r}) = \left[\frac{\chi(\tilde{r}) - 1}{\chi(\tilde{r}) + 1} \right]^2, \quad (13)$$

When evaluating this expression one would immediately see that the critical shell radius \tilde{r}_{cs} is an increasing function of Ω_{Λ} . Also, as expected, the shell would reach its maximum – turnaround – radius r_{\max} at $t \rightarrow \infty$.

For the cosmology at hand ($\Omega_{m,0} = 0.3$, $\Omega_{\Lambda,0} = 0.7$) the critical shell currently has a dimensionless radius $\tilde{r}_0 = 0.84$. In other words, the critical shell has a present radius that is 84% of its maximum radius.

2.4 Conditions for a critical shell

For practical applications, it is convenient to express the critical condition as the minimum enclosed mean density needed by a shell to stay bound to the central spherical mass concentration.

The critical density of the Universe is

$$\rho_c = \frac{3H^2}{8\pi G}, \quad (14)$$

and the average mass density enclosed by a given shell is

$$\bar{\rho}_s = \frac{3M}{4\pi r^3}. \quad (15)$$

Evaluating for each shell the ratio between the average mass density enclosed by the shell and the critical density is

$$\frac{\bar{\rho}_s}{\rho_c} = \frac{2\Omega_{\Lambda}}{\tilde{r}^3}. \quad (16)$$

the condition for the shell to be bound is simply

$$\frac{\bar{\rho}_s}{\rho_c} \geq \frac{\rho_{cs}}{\rho_c} = \frac{2\Omega_{\Lambda}}{\tilde{r}_{cs}^3} = 2.36, \quad (17)$$

where the value corresponds to a Universe with $\Omega_{\Lambda,0} = 0.7$. For the latter we used that the current dimensionless radius of the critical shell is $\tilde{r}_0 = 0.84$ (see sec. 2.3). Note that for $\Omega_{\Lambda} = 1$ ($t \rightarrow \infty$) the critical shell's density is $\rho_{cs}/\rho_c = 2$. This is the density value it reaches at its maximum radius.

A closely related quantity is the density excess δ of the spherical mass concentration with respect to the global cosmic background. The uniform cosmic matter density $\rho_u(t)$ evolves according to

$$\rho_u(t) = \frac{\rho_{c,0} \Omega_{m,0}}{a^3}, \quad (18)$$

where $\rho_{c,0}$ and $\Omega_{m,0}$ are the critical density and matter density parameters at the present epoch. Using this expression, the density excess of the spherical density concentration can be inferred from

$$1 + \delta \equiv \frac{\rho}{\rho_u} = \frac{2\Omega_{\Lambda,0}}{\Omega_{m,0}} \left(\frac{a}{\tilde{r}} \right)^3. \quad (19)$$

On the basis of this equation we find that the a critically bound shell at the present epoch involves a density excess in the order of $\delta_{cs} \approx 6.9$.

2.5 Bound Object: linearly extrapolated density threshold

To be able to identify the primordial regions that correspond to bound, collapsing and/or virialized objects at any arbitrary redshift z we need the value of the corresponding linearly extrapolated densities. For the current study it is also needed to enable a comparison of the simulation object mass functions with the analytical predictions of the Press-Schechter and Sheth-Tormen mass functions (see appendix A).

According to gravitational instability theory (Peebles

1980), in the linear regime the density excess $\delta(a)$ simply grows as

$$\delta(a) = D(a) \delta_0 \quad (20)$$

where $D(a)$ is the linear density growth factor (growing mode). In a FRW universe with matter and a cosmological constant, it can be computed from (Heath 1977; Peebles 1980)

$$D(a) \equiv ag(a) = \frac{5\Omega_{m,0}H_0^2}{2} H(a) \int_0^a \frac{da'}{a'^3 H(a')^3} \quad (21)$$

where $g(a)$ is the growth with respect to that in an Einstein-de Sitter Universe ($D(a)$ is normalized such that $D(a) \approx a$ for $a \downarrow 0$). In an EdS Universe linear structure growth is linearly proportional to the cosmic expansion factor, $D(a) = a$. In order to find the linear density excess δ_0 for the criti-

cally bound shell, we return to its evolution at early epochs ($a \ll 1$). At these early times – when density perturbations are still very small, $\delta \ll 1$ – the linearly extrapolated density excess (eqn. 20) represents a good approximation for the (real) density of the object (eqn. 17).

At early times the Universe is very close to an Einstein-de Sitter Universe and expands accordingly,

$$a(t) = \left(\frac{t}{t_*} \right)^{2/3}, \quad (22)$$

where t_* is the characteristic expansion time. Following this cosmic evolution, the implied development of the density perturbation δ can be determined from equation (19). Up to first order, it yields the relation

$$\frac{t(\tilde{r})}{\tilde{r}^{3/2}} \approx t_* \left(1 + \frac{\delta}{2} \right) \left(\frac{\Omega_{m,0}}{2\Omega_{\Lambda,0}} \right)^{1/2}. \quad (23)$$

This approximation, neglecting contributions of order δ^2 and higher, is reasonably accurate for density perturbations $\delta \ll 1$. The evolution of the critical shell's radius $\tilde{r}(t)$ is given by the integral expression eqn. (10). Retaining the two lowest order terms,

$$t(\tilde{r}) \approx \sqrt{\frac{2}{3\Lambda}} \tilde{r}^{3/2} + \frac{3}{10} \sqrt{\frac{3}{2\Lambda}} \tilde{r}^{5/2}, \quad (24)$$

we find that

$$\frac{t}{\tilde{r}^{3/2}} \approx \sqrt{\frac{2}{3\Lambda}} \left(1 + \frac{9}{20} \tilde{r} \right). \quad (25)$$

Note that the front factor on the righthand side of this equation should be equal to that of eqn. (23), so that the characteristic time t_* is found to be

$$t_* = \left[\frac{4\Omega_{\Lambda,0}}{3\Lambda\Omega_{m,0}} \right]^{1/2}. \quad (26)$$

Combining expression (24) with that of eqn. (23) we find that

$$t_* \left(1 + \frac{\delta}{2} \right) \left(\frac{\Omega_{m,0}}{2\Omega_{\Lambda,0}} \right)^{1/2} \approx \sqrt{\frac{2}{3\Lambda}} \left(1 + \frac{9}{20} \tilde{r} \right) \quad (27)$$

resulting in the following relation between the early density

excess of the bound sphere and its dimensionless radius \tilde{r} is

$$\delta(t) = \frac{9}{10} \tilde{r}(t). \quad (28)$$

Finally, using the approximate evolution of $\tilde{r}(a) \propto a$ implied by eqn. (19), for early times ($1 + \delta \approx 1$) we have

$$\delta(t) = \frac{9}{10} \left(\frac{2\Omega_{\Lambda,0}}{\Omega_{m,0}} \right)^{1/3} a(t). \quad (29)$$

The above leads us directly to the value of the linear density excess δ_0 , as at the early Einstein-de Sitter phase $\delta(t) \approx a(t)\delta_0$,

$$\delta_0 = \frac{\delta}{a} = \frac{9}{10} \left(\frac{2\Omega_{\Lambda,0}}{\Omega_{m,0}} \right)^{1/3} \approx 1.504. \quad (30)$$

The corresponding linearly extrapolated density excess for marginally bound structures at the present epoch is

$$\delta_b(a=1) = 1.17 \quad (31)$$

where we have used the approximation for $g(a) = D(a)/a$ (Carroll et al. 1992)

$$g(a) \approx \frac{5}{2} \Omega_m(a) \times \left[\Omega_m(a)^{4/7} - \Omega_\Lambda(a) + \left(1 + \frac{\Omega_m(a)}{2} \right) \left(1 + \frac{\Omega_\Lambda(a)}{70} \right) \right]^{-1} \quad (32)$$

These objects are due to collapse at $a \rightarrow \infty$.

2.6 Tests Spherical Binding Criteria

Reality is always far more complex than a simple analytical criterion is liable to cover. In addition to distinct anisotropies, internal inhomogeneities and velocity dispersions will influence the viability of the derived spherical binding criterion. By means of N-body simulations Dünner et al. (2006) tested the binding density criterion $\rho_{cs}/\rho_c = 2.36$ (for the current epoch) and the criterion involving the mass enclosed within the radius r_{cs} . On average 72% of the mass enclosed within r_{cs} is indeed gravitationally bound to the structure. At the same time it was found that a mere 0.3% of the mass bound to the object is not enclosed within this radius.

3 THE COMPUTER SIMULATION

We simulate one cosmological model, assuming a standard flat Λ CDM Universe. The cosmological parameters in the simulation are $\Omega_{m,0} = 0.3$, $\Omega_{\Lambda,0} = 0.7$, and $h = 0.7$, where the Hubble parameter is given by $H_0 = 100h \text{ km s}^{-1} \text{ Mpc}^{-1}$, and the normalization of the power spectrum is $\sigma_8 = 1$. In order to have a large sample of bound objects, the simulation box has a side length of $500h^{-1} \text{ Mpc}$ and contains 512^3 dark matter particles of mass $m_{dm} = 7.75 \times 10^{10} h^{-1} \text{ M}_\odot$. The initial conditions were generated at expansion factor $a = 0.02$ (redshift $z = 49$), and were evolved until $a = 100$ using the massive parallel tree N-Body/SPH code GADGET-2 (Springel 2005). The Plummer-equivalent softening was set at $\epsilon_{PI} = 20 h^{-1} \text{ kpc}$ in physical units from $a = 1/3$ to $a = 100$, while it was taken to be fixed in comoving units

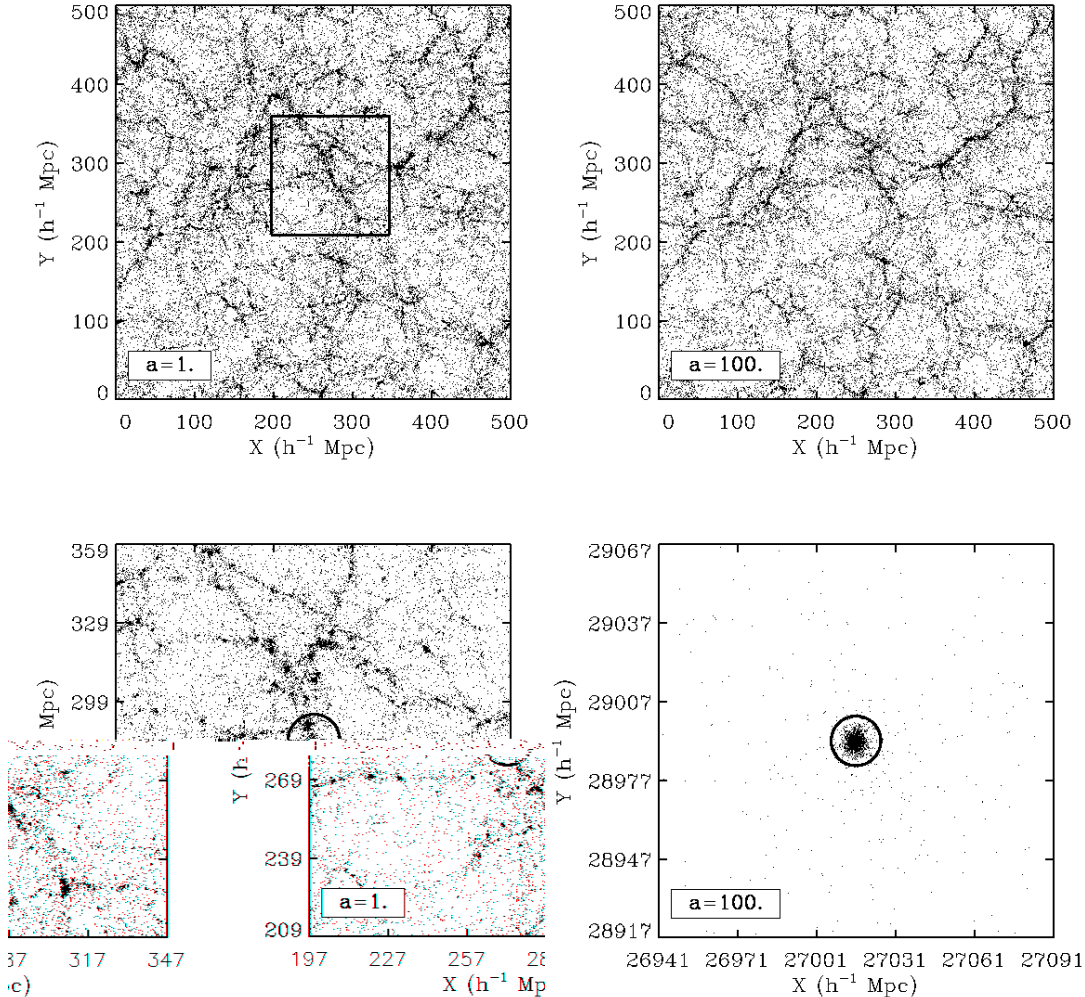


Figure 1. Simulation mass distribution at $a = 1$ (left column) and $a = 100$ (right column). The top row panels show the particle distribution in a $500h^{-1}\text{Mpc}$ box. Both panels show the particle positions in a $30h^{-1}\text{Mpc}$ thick slice projected along the z -axis. Top left: mass distribution at $a = 1$. Top right: mass distribution at $a = 100$. Lower left: zoom-in on the $a = 1$ mass distribution within $50h^{-1}\text{Mpc}$ box indicated by the square in the top lefthand panel (similar $30h^{-1}\text{Mpc}$ thick slice along z direction). Lower right: region of same $50h^{-1}\text{Mpc}$ physical size as the lower left panel, at $a = 100$, around the same bound supercluster (physical width of slice is $30h^{-1}\text{Mpc}$). By taking a region of the same physical size, the effect of the de Sitter expansion of the Universe is manifestly clear.

at higher redshift. Given the mass resolution and the size of the box, our simulation allows us to reliably identify massive superclusters with $\sim 80,000$ particles. The simulation was performed on the Beowulf Cluster at the University of Groningen.

We took snapshots at the present time ($a = 1$) and in the far future ($a = 100$). We take $a = 100$ as the representative epoch at which the internal evolution of all bound objects has been completed.

3.1 Identification of bound objects and superclusters

For the identification of bound structures in the simulations, we apply a three-step procedure. In the first step, we find all virialized halos in the simulations with more than 50 particles. Subsequently, we incorporate the surrounding spherical

region bound to these halos. We then join the bound spheres that overlap each other into single bound objects. Finally, among these objects we select the most massive ones, the superclusters in the simulation volume.

3.1.1 Mass range

A first practical issue is the minimal amount of particles we deem necessary to accept a halo/object detection as significant. We choose a minimum of 50 particles, corresponding to a mass cut of $M \geq 3.1 \times 10^{13} h^{-1} M_{\odot}$. This means our cluster and bound object sample has an implicit bias in not containing any objects with a mass less than the mass limit. This is not a problem for the most massive objects, but may produce an incomplete sample for lower mass objects.

3.1.2 HOP and virialized halo finding

In order to find groups of particles present in our simulation, we use HOP (Eisenstein & Hut 1998). This algorithm first assigns a density estimate at every particle position by smoothing the density field with an SPH-like kernel using the n_{dens} nearest neighbors of a given particle. In our case, we use $n_{dens} = 64$. Subsequently, particles are linked by associating each particle to the densest particle from the list of its n_{hop} closest neighbors. We use $n_{hop} = 16$. The process is repeated until it reaches the particle that is its own densest neighbor. Note that we extract the virialized groups in the simulation on the basis of a random subsample of 256^3 particles (1/8 of the total particle number).

The algorithm associates all particles to their local maxima. This procedure often causes groups to fragment. To correct this, groups are merged if the bridge between them exceeds some chosen density thresholds. Three density thresholds are defined as follows (Cohn et al. 2001):

- δ_{out} :
the required density for a particle to be in a group.
- δ_{saddle} :
the minimum boundary density between two groups so that they may have merged.
- δ_{peak} :
the minimum central density for a group to be independently viable.

We follow the criterion of Eisenstein & Hut (1998) $\delta_{outer}:\delta_{saddle}:\delta_{peak}=1:2.5:3$. We associate the value of δ_{peak} with that of the corresponding virial density $\Delta_{vir}(z)$ of the virialized core of the bound regions.

Virial Density Value

To determine the value of the virial density $\Delta_{vir}(z)$ in the HOP formalism we resort to the dynamical evolution of spherical top-hat perturbation. We need to distinguish between the situation at $a = 1$ and $a = 100$.

The value of $\Delta_{vir}(z)$ at $a = 1$ is taken from the solution to the collapse of a spherical top-hat perturbation under the assumption that the object has just virialized. Its value is $18\pi^2$ for an Einstein-de Sitter Universe, and has to be evaluated numerically for other cosmologies (Gunn & Gott 1972; Lacey & Cole 1993; Eke et al. 1996; Kitayama & Suto 1996; Bryan & Norman 1998). A good approximation for the case of a flat Universe ($\Omega_m + \Omega_\Lambda = 1$) was found by Bryan & Norman (1998),

$$\Delta_{vir}(z) \approx \frac{18\pi^2 + 82x - 39x^2}{1 + x} \quad (33)$$

where $x = \Omega_m(z) - 1$. This relation is accurate in the range $\Omega_m(z) = 0.1 - 1$. For the cosmology described here, $\Delta_{vir} \approx 337$. Note that this value is with respect to the background density ρ_u of the Universe, not the critical density ρ_c .

At $a = 100$, $\Omega_m = 4.3 \times 10^{-7}$. This means that the approximation by equation 33 is no longer valid and cannot be applied. To determine the characteristic virial radius we resort directly to the virial theorem itself.

According to the virial theorem the kinetic energy K_{vir} of a body whose potential is of the form $V_{vir} = R^n$ is equal

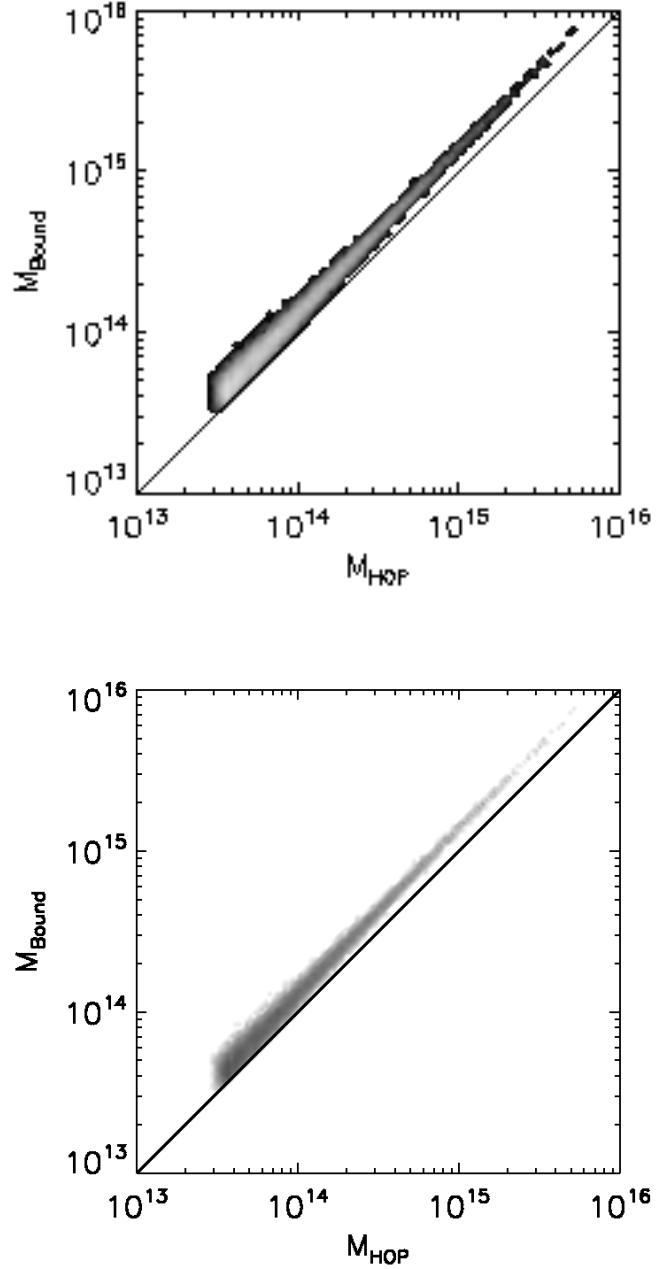


Figure 2. Scatter plots of the mass of identified bound objects, M_{bound} , against the mass of the virialized HOP halo that forms its core, M_{HOP} . The density of points (M_{HOP}, M_{Bound}) in the scatter diagram is depicted in terms of an isodensity contour map. The highest concentration of points has the darkest (black) shade, gradually fading towards light colours. Top: $a = 1$. Bottom: $a = 100$

to $K_{vir} = (n/2)V_{vir}$ (Landau & Lifschitz 1960; Lahav et al. 1991). For a general case of a virialized object in a Universe with matter and a cosmological constant

$$K_{vir} = -\frac{1}{2}\tilde{V}_{G,vir} + \tilde{V}_{\Lambda,vir} \quad (34)$$

where \tilde{V}_G is the gravitational potential energy and \tilde{V}_Λ is the potential energy due to the cosmological constant (Lahav et al. 1991). Hence, the total energy $E_{vir} = K_{vir} +$

V_{vir} of a virialized object is

$$\tilde{E}_{vir} = \frac{1}{2}\tilde{V}_{G,vir} + 2\tilde{V}_{\Lambda,vir} \quad (35)$$

Because of energy conservation, the energy at maximum expansion is equal to the energy at virialization. This translates into the following equation for the dimensionless radius

$$\tilde{r}^2 + \frac{1}{2\tilde{r}} = \frac{3}{2}. \quad (36)$$

This is a cubic equation with solutions $\tilde{r} \approx -1.366$, $\tilde{r} = 1$ and $\tilde{r} \approx 0.366$. The first is an unphysical solution. The solution $\tilde{r} = 1$ is the maximum radius of the critically bound shell (see eqn. 2.4). The third value, $\tilde{r} \approx 0.366$, is the virial radius of the enclosed mass M . The corresponding virial density excess of the mass clump would be $1 + \Delta_{vir} = \bar{\rho}/\rho_c \approx 40.8$ (eqn. 16).

3.1.3 Clusters

Besides the definition of a sample of superclusters, we also identify the clusters in our simulation. Their identity is more straightforward to define, given we may presume they are virialized.

Virialized halos, as identified by HOP (sect. 3.1.2), with masses larger than $3 \times 10^{13} h^{-1} M_{\odot}$, are considered *clusters*. Note that, by definition, these clusters are identical to the bound object cores produced in step 1 of our supercluster finding procedure (sect. 3.1.2).

3.1.4 Bound Halo Identification

Once we have identified the virialized halos in our sample, we have to proceed by outlining the gravitationally bound region around these cores and, if necessary, join them together into a supercluster. In practice, we do this as follows.

Of an identified HOP halo, we take the location of the densest particle as a first estimate of the center of mass. Subsequently, we grow a sphere around this center, with the radius being increased until the mean overdensity within the corresponding radius reaches a value of $300\rho_c$. This value is chosen in order to find the densest core of the structure. We then calculate the center of mass of this sphere and repeat the process, iterating until the shift in the center between successive iterations is less than 1% of the radius.

With the final center of mass, we apply the criterion of Eqn. 17 for identifying the bound spherical region around the HOP core, i.e. we find the radius r_{cs} within which the average interior density at $a = 1$ is $\rho_{cs}/\rho_c = 2.36$ and at $a = 100$ is $\rho_{cs}/\rho_c = 2$. (see sect. 2.4).

3.1.5 Joining Halos: Bound Objects

The procedure outlined in the previous paragraph will frequently lead to overlapping bound spheres that in reality will be bound to each other. In order to account for this, we follow a radical prescription. If two spheres overlap, we proceed with the most massive one and join the lower mass sphere to the high mass one while removing it from the list of objects.

We found that by following this procedure at $a = 100$, such overlaps do not occur. It implies that in the far future

nearly all bound objects are compact and isolated islands in the Universe. At $a = 1$, it does turn out to occur for a significant fraction of the bound spheres.

3.1.6 Superclusters and Bound Objects

Because not all bound objects would be prominent enough to be a supercluster, we use a mass threshold to select the superclusters amongst the bound objects in our sample. The mass threshold is chosen to be $M_{sc} = 10^{15} h^{-1} M_{\odot}$, approximately the mass of the Local Supercluster. Although its value is somewhat arbitrary, and perhaps a somewhat different value might also have been viable, it represents a reasonable order of magnitude estimate.

As a result we reserve the name *bound objects* for all the objects that have ended up in our sample, while *superclusters* are the subset with masses higher than our supercluster mass threshold of $10^{15} M_{\odot}$.

3.1.7 Sample completeness

Fig. 2 helps us to evaluate the completeness of our object sample. The panels contain scatter plots of the total mass of the bound objects versus the HOP mass of their corresponding virialized cores.

Evidently, the lower right region is empty: HOP groups will always be less massive than the bound groups. There is a correlation between both masses, but with a high scatter. As expected, the correlation is substantially stronger at $a = 100$ than at $a = 1$. On the basis of these relations, we may conclude that at $a = 1$ the sample is complete for masses greater than $2 \times 10^{14} h^{-1} M_{\odot}$, while at $a = 100$ the sample is complete for masses down to $6 \times 10^{13} h^{-1} M_{\odot}$. In order to keep the samples comparable, we use a mass completeness threshold of $2 \times 10^{14} h^{-1} M_{\odot}$ at $a = 1$ and $1.4 \times 10^{14} h^{-1} M_{\odot}$ at $a = 100$ (see discussion sect. 4).

3.2 Results

The top two panels of Fig. 1 show a slice of $30h^{-1}$ Mpc width of the particle distribution projected along the z axis, both at $a = 1$ and $a = 100$. At $a = 1$, the large-scale structure of the cosmic web is well established. Its morphology and character hardly changes thereafter.

The lower left panel zooms in on the square region of the top-left panel. Centered on a massive structure, it shows the mass distribution at $a = 1$. The radius of the circle is that of the bound region, according to the criterion of Eqn. 17. It shows that it is well connected with the surrounding structure. The same object, but now at $a = 100$, is depicted in the lower right panel (with the same *physical scale*). We see that the size of the bound object is nearly the same at both expansion factors. While in comoving coordinates the accelerated expansion of the Universe results in a freezing of structure growth, in physical coordinates the separation of structures continues and grows exponentially in time. This results in clearly detached regions which evolve in complete isolation: genuine *cosmic islands*.

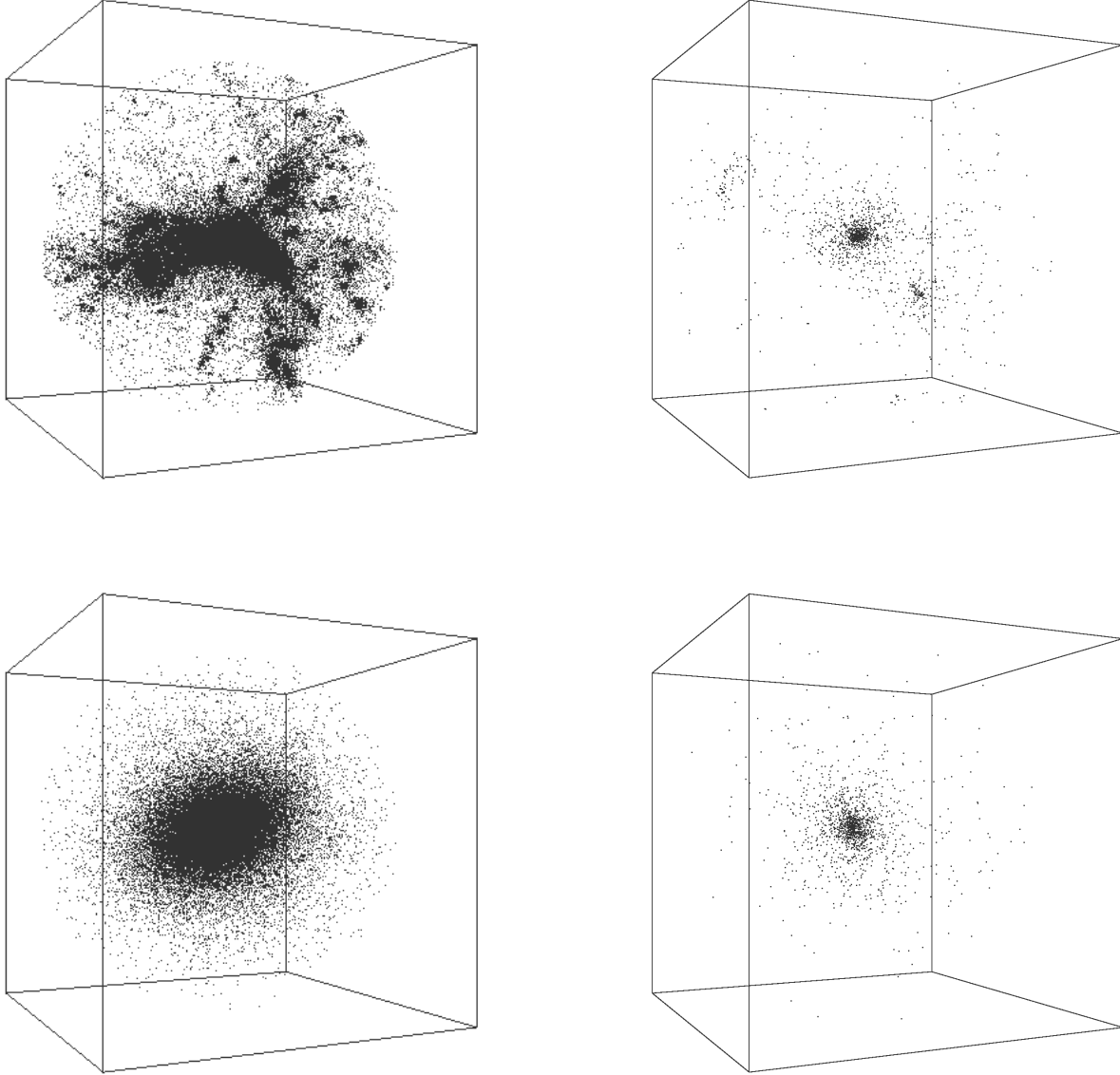


Figure 3. Two examples of bound objects in our simulation. Top row: the objects at $a = 1$. Bottom row: the objects at $a = 100$. The particle positions are in comoving coordinates. Lefthand column: one of the most massive objects in our simulation, with a present-day mass $M \sim 6.8 \times 10^{15} h^{-1} M_{\odot}$, at $a = 1$ (top) and at $a = 100$ (bottom). The size of the box is $14 h^{-1} \text{Mpc}$. Righthand: the configuration of one of the least massive bound objects, with a present-day mass of $\sim 2 \times 10^{14} h^{-1} M_{\odot}$ (boxsize at $a = 1$: $4 h^{-1} \text{Mpc}$, boxsize at $a = 100$: $3 h^{-1} \text{Mpc}$). Note the strong change of the massive object, in contrast to the marginal evolution of the low mass one.

3.2.1 The Object Sample

HOP finds ~ 20600 independently virialized groups at $a = 1$ and ~ 18000 at $a = 100$ with more than 50 particles, i.e. halos with a total mass $M \geq 3.1 \times 10^{13} h^{-1} M_{\odot}$. These will be taken as the starting point for our supercluster finding procedure. They also constitute the cluster sample in our simulation.

After determining the connected bound region and joining these overlapping bound spheres (see sec. 3.1.5), plus checking for sample completeness, we finally end up with a sample ~ 4900 bound objects at the current epoch. At

$a = 100$ this is approximately the same number. Of these ~ 535 are superclusters (at $a = 1$), while seventeen are truly massive supercluster complexes with $M_{sc} > 5 \times 10^{15} h^{-1} M_{\odot}$.

3.2.2 Objects Sample: examples

Two representative examples of the bound objects in our sample are shown in Fig. 3. It shows the two objects at $a = 1$ (top row) and at $a = 100$ (bottom row). The object on the left is amongst the most massive objects, a supercluster with a mass of $\sim 6.8 \times 10^{15} h^{-1} M_{\odot}$ (at $a = 1$). The righthand

object is one of the least massive ones in our sample, and has a mass of $\sim 2 \times 10^{14} h^{-1} M_{\odot}$.

At $a = 1$ the massive supercluster (Fig. 3, lefthand) is marked by a substantial degree of substructure. The centre of the supercluster is dominated by the massive central cluster that is the virialized object from which we constructed the remainder of the supercluster. It forms the centre of a huge complex, connecting the surrounding matter distribution via prominent filamentary extensions. These form the transport channels along which mass flows into the central supercluster region. Noteworthy is the large number and variety of subclumps along the filaments and around the centre of the supercluster.

The moderate low-mass bound object (Fig. 3, righthand) hardly shows any substructure and seems to consist only of a central region and a few particles within the binding radius. Although to some extent this may be a consequence of the limited resolution of our simulation, the fact that it hardly changed in appearance towards $a = 100$ (Fig. 3, lower righthand) is an indication for a systematic trend.

By contrast, we see a radical change of the high mass supercluster. It has turned into a highly concentrated, regular, and nearly ellipsoidal mass clump. All substructure within its radius has fallen in and has been absorbed into one big mass concentration.

4 SUPERCLUSTER MASS FUNCTIONS

With the identification of superclusters we may ask how much mass is contained in them at the present epoch and at $a = 100$. At $a = 1$, the entire sample of bound objects in our simulation box amounts to $2.73 \times 10^{18} h^{-1} M_{\odot}$. At $a = 100$ this has grown to a total mass of $2.83 \times 10^{18} h^{-1} M_{\odot}$. This represents 26%, respectively 27%, of the total mass in our simulated Universe ($1.04 \times 10^{19} h^{-1} M_{\odot}$).

We may make two immediate observations. First, given that bound objects tend to lose around 28% of their mass towards $a = 100$ (see below), it must mean that the number of bound objects fulfilling our criterion - of containing one or more virialized cores - is still growing from $a = 1$ towards $a = 100$. It may also indicate a problem in applying a purely spherical density criterion: at $a = 1$ mass concentrations are more aspherical and inhomogeneous, while at $a = 100$ they are nearly spherical concentrated mass concentrations (see sec. 5). Perhaps even more tantalizing is the fact that apparently more than 70% of mass in the Universe will remain outside of the supercluster islands and will keep on floating as a lonely population of low mass objects in a vast cosmic void.

Perhaps the most outstanding repercussion of the slow-down of large scale structure formation in hierarchical cosmological scenarios is the fact that the condensation of new objects out of the density field will gradually come to a halt. This should be reflected in the mass spectrum of the objects that were just on the verge of formation around the time of the cosmological transition. Here we investigate the mass distribution of superclusters, ie. bound but not yet fully virialized structures. For comparison we also investigate a sample of virialized halos.

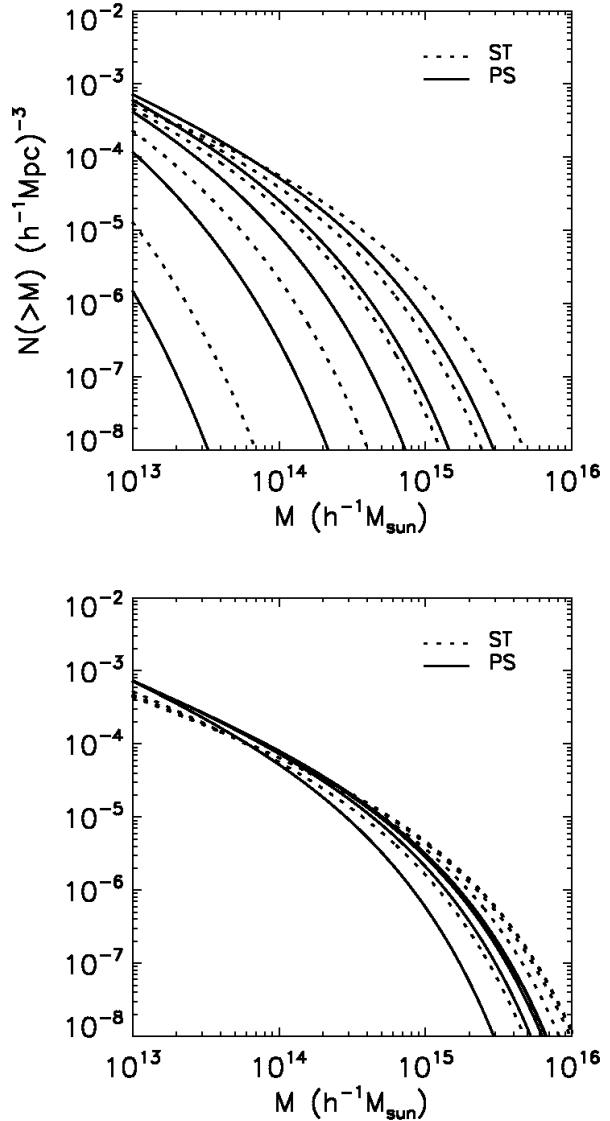


Figure 4. Theoretical mass functions for virialized objects in a Λ CDM Universe ($\Omega_{m,0} = 0.3, \Omega_{\Lambda,0} = 0.7, h = 0.7$). Shown are the Press-Schechter mass functions (dashed lines) and the Sheth-Tormen mass functions (solid lines). Top: the mass functions at redshifts $z = 4, 2, 1, 0.5$ and 0 (from left to right). Bottom: the mass functions at expansion factors $a = 1, 2, 4, 10$ and 100 (from left to right).

4.1 Theoretical mass functions

Fig. 4 shows the evolution of the mass function of virialized objects predicted by the Press-Schechter formalism (Press & Schechter 1974) and the Sheth-Tormen excursion set prescription (Sheth & Tormen 1999), for the current cosmology. The Sheth-Tormen expression takes into account the anisotropic collapse of dark halos. We also compare our mass functions to the heuristic simulation-based mass function suggested by Jenkins et al. (2001). We refer to appendix A for a listing of the expressions for these mass functions.

The lefthand panel shows the strong evolution in the

past, by depicting the mass functions at $z = 4, 2, 1, 0.5$ and 0. It shows that structure grows in mass and number while the Universe expands. The future evolution is a lot less strong, as evidenced by the mass functions at expansion factors $a = 1, 2, 4, 10$ and 100 in the righthand panel. After $a = 1$ the number of low mass objects does not change substantially, while after $a = 4$ evolution comes to a complete halt. This may be best appreciated from the fact that the curves for $a = 10$ and $a = 100$ overlap completely.

We see that the Sheth-Tormen approximation predicts a higher number of massive clusters than the Press-Schechter formalism. As anisotropic collapse speeds up the contraction along the minor axis of an object, there is a higher number of regions reaching a sufficiently large overdensity before dark energy prevents any further evolution. Implicitly, this lowers the number of low-mass objects as more get absorbed into the high mass superclusters.

4.2 Simulation mass functions

We assess the mass function of the virialized halos, the objects identified by HOP on the basis of the prescription in sec. 3.1.2, and that of that of the bound (supercluster) objects that were identified according to the criterion specified in section 3.1.

Fig. 5 shows the mass functions of the virialized halos found by HOP (left panel) and of the bound objects (central panel), at $a = 1$ and $a = 100$. As expected, the number of massive virialized halos increases as we go from $a = 1$ to $a = 100$. The increase is only marginal, yet significant, and a manifestation of the freezing of structure formation and hence that of the corresponding mass functions (see also Nagamine & Loeb 2003). The mass functions at $a = 1$ and $a = 100$ also reflect the continuing hierarchical evolution within the realm of the bound supercluster regions. There is a definitive increase in the number of the most massive clumps, going along with a decrease at the low-mass side of the mass function.

When turning towards the mass function for the bound (supercluster) regions (central panel) we do find the same mass function at $a = 1$ and $a = 100$, except for a slight decrease in the mass of the objects over the whole mass range. There is a loss of mass, amounting to some $28 \pm 13\%$ of the mass enclosed within the critical radius of the superclusters at $a = 1$. This is substantially more than the mere 1% mass gain as a result of accretion of mass in between $a = 1$ and $a = 100$. The loss of mass has to be ascribed to the virialization process of and within the bound object. A major factor in this is the abundant substructure in the supercluster at the present epoch as opposed to the smoothed mass distribution within the ultimate supercluster island at $a = 100$. In order to correct for this ‘‘reduced’’ mass we renormalize the supercluster mass function into a *reduced* supercluster mass function, simply by multiplying the masses by a factor 0.72. As may be observed in the righthand panel of fig. 5 we find an almost perfect overlap between the mass function at $a = 100$ and its reduced equivalent at $a = 1$.

4.3 Comparison simulated and theoretical mass functions

Fig. 6 shows the cumulative mass function of the virialized objects found by HOP at $a = 1$ (left panel) and at $a = 100$ (central panel), together with three theoretical mass functions (see app. A). The righthand panel compares the mass function, at $a = 1$, of the bound (supercluster) regions in our simulation with the theoretical mass functions. The mass function for these bound objects at $a = 100$ is slightly shifted to lower masses (see fig. 5).

4.3.1 Mass functions of bound objects and superclusters

To compare the mass function of the bound (supercluster) regions with the theoretical Press-Schechter and Sheth-Tormen functions we need to specify a critical overdensity corresponding to the bound (supercluster) regions in our sample (see app. A). Because the bound (supercluster) regions in this study are assembled on the presumption that they are marginally bound, we use the corresponding value of the linear extrapolated density excess, $\delta_b = 1.17$, derived in section 2.5 (see eqn. 31).

It is interesting to note that at $a = 1$ the Sheth-Tormen function seems to provide a better fit than the Press-Schechter function to the bound object mass spectrum, in particular for the tail of massive superclusters. It demonstrates the importance of morphological and tidal influences on the mass spectrum of these generically nonspherical objects (see next section 5). We also found that at $a = 100$ the Press-Schechter function provides a substantially better fit to the bound object mass function. This may be related to the fact that the PS formalism implicitly assumes pure spherical collapse, which we will see in sect. 5 agrees quite well with the shape of superclusters at $a = 100$. Also, we find that in the far future, when most of our superclusters have become isolated and largely virialized islands, it is appropriate to compare with a Press-Schechter or Sheth-Tormen mass function based on another critical density value. At $a = 100$ most *cosmic islands* will reside in a dynamical phase somewhere between marginally bound and full collapse, implying a critical value in between $\delta_b = 1.17$ (eqn. 31) and the collapse threshold $\delta_c = 1.675$ (eqn. A4).

It is also clear that the Jenkins function does not provide a suitable fit to the supercluster mass function. This may not be surprising given the fact that it is a numerical approximation of the mass function of collapsed and virialized halos in N-body simulations and as such does not explicitly include an adjustable density threshold δ_c .

4.3.2 Cluster mass function

It is more straightforward to compare the mass function of the clusters, or HOP halos, in our simulation with that of the three theoretical mass functions for virialized objects. For these fits we use the critical collapse density value $\delta_c = 1.675$, the value for our cosmology according to eqn. A4. The Jenkins approximation is of course independent of the value of δ_c .

At $a = 1$ the Jenkins mass function (Jenkins et al. 2001) is the one that fits best (dot-dashed line), perhaps not entirely surprising given its N-body simulation background.

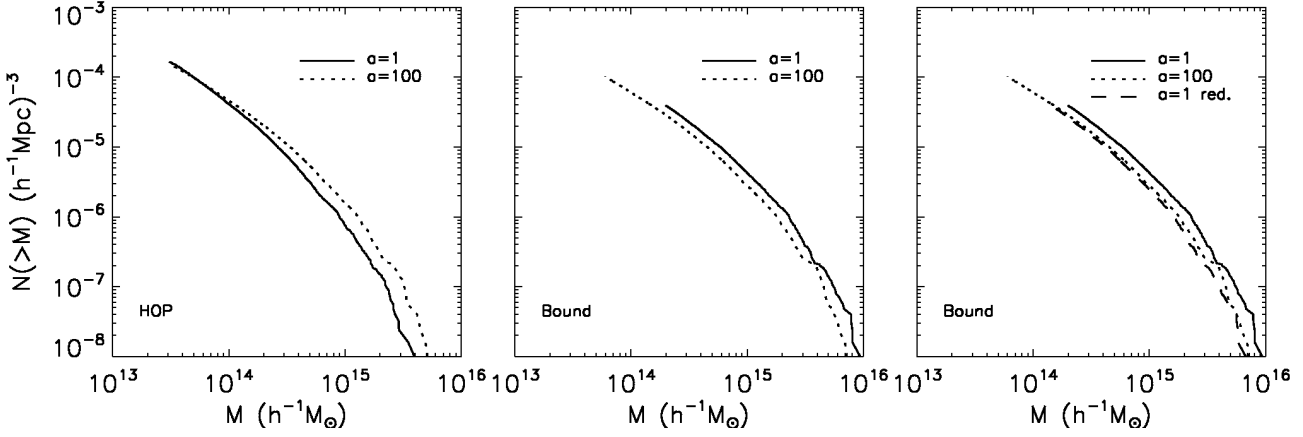


Figure 5. Mass functions of virialized halos and of bound objects. Left: integrated mass function $N(>M)$ for virialized HOP objects in the simulation, at $a = 1$ (solid line) and $a = 100$ (dotted line). Centre: integrated mass function $N(>M)$ for bound objects in the simulation, at $a = 1$ (solid line) and $a = 100$ (dotted line). Right: the integrated mass function $N(>M)$ for bound objects compared with the *reduced* $a = 1$ mass function (dashed line). See text for explanation.

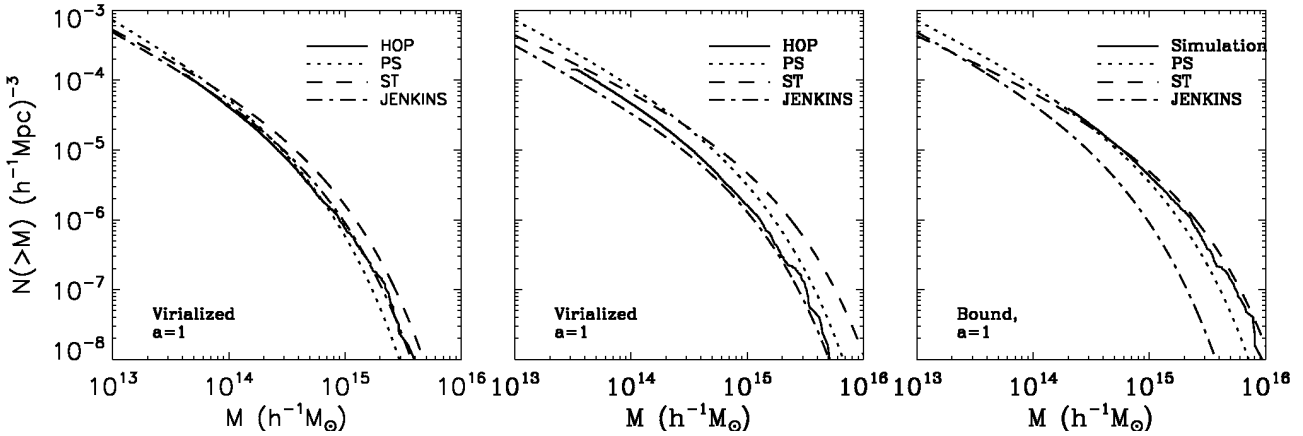


Figure 6. Mass functions of virialized halos and of bound objects compared with three theoretical mass functions. These are the Press-Schechter mass function (dotted line), the Sheth-Tormen function (dashed line) and the Jenkins function (dot-dashed line). For the virialized HOP halos the critical overdensity δ_c for the PS and ST functions is the one for collapse, for the bound objects the value δ_b for assuring a bound object (Dünner et al. 2006, this study). Left panel: the $a = 1$ integrated mass function $N(>M)$ of HOP halos. Centre: the $a = 100$ integrated mass function $N(>M)$ of HOP halos. Righthand: the $a = 100$ integrated mass function $N(>M)$ of bound objects.

The Press-Schechter mass function represents a good fit at the lower mass end, although it underestimates the number of high mass clusters. Governato et al. (1999) claim that a critical density value $\delta_c = 1.775$ would provide a better fit and indeed it would lead to a small yet significant improvement of the Sheth-Tormen mass function.

For $a = 100$ we adjust the parameters of the Jenkins function, using the fitting parameters for $\Omega_m = 0$ listed in Evrard et al. (2002). With these parameters, it agrees very well with the HOP mass function, although it slightly overestimates the number of lower mass objects. However, for Jenkins' original parameter values, it would lead to a significant overabundance of objects with respect to the ones found in the simulations.

Neither the pure Press-Schechter nor the Sheth-Tormen function manage to fit the mass spectrum at $a = 100$ over the entire mass range. Press-Schechter does agree at the high mass end while Sheth-Tormen results in a better agreement

at lower masses. This may be an indication for the more substantial role of external tidal forces on the evolution of the low mass halos. Such external influences are entirely ignored by the Press-Schechter formalism, while they are successfully modelled by the Sheth-Tormen fits (Sheth & Tormen 1999).

5 SHAPES OF BOUND STRUCTURES

While the large scale formation and evolution of structure comes to a halt once the Universe starts to accelerate, the internal evolution of overdense patches continues. Perhaps the most telling manifestation of this is the changing shape of these collapsing objects.

As the expansion of the Universe enters into an accelerating phase, the bound structures become increasingly isolated. No major mergers between structures happen after $a = 1$. The substructures that are within the bound radius

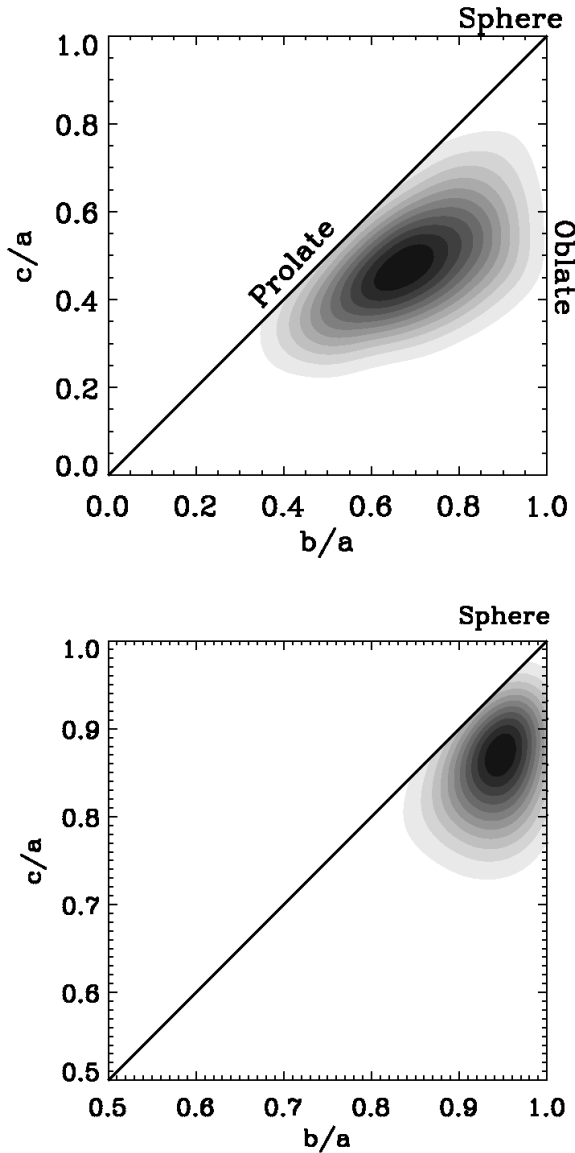


Figure 7. Distribution of axis ratios for bound objects at $a = 1$ (top panel) and at $a = 100$ (bottom panel). Each diagram shows the probability density distribution in the plane of b/a versus c/a values, with principal axes $c < b < a$. Plotted is the axis ratio probability distribution in iso-probability greyscale values. Dark colors correspond to high probability, decreasing to lower probability as colours fade to light. The shape evolution towards more spherical objects is clearly visible, with a slight tendency towards prolate shapes.

will merge with each other into an increasingly smooth and concentrated clump that will gradually assume a more and more spherical configuration.

Using a variety of definitions for superclusters, their shape has been studied both using real data (e.g. Plionis et al. 1992; Sathyaprakash et al. 1998; Basilakos et al. 2001; Sheth, Sahni, Shandarin 2003; Einasto et al. 2007) and in N-Body simulations (e.g. Sathyaprakash et al. 1998; Shandarin et al. 2004; Basilakos et al. 2006; Wray et al. 2006; Einasto et al.

2007). Most studies agree that the dominant shape of superclusters at the present time is prolate, most evident in the presence of elongated filaments. These predominantly anisotropic shapes are a clear indication for the quasi-linear dynamical stage at which we find the present-day superclusters.

5.1 Definitions

In order to determine the shape, we calculate the inertia tensor using all particles inside the spheres defined by Eqn.17 with respect to their center of mass:

$$I_{ij} = \sum x_i x_j m. \quad (37)$$

Since the matrix is symmetric, it is possible to find a coordinate system such that it is diagonal, yielding the eigenvalues a_1 , a_2 and a_3 . These give a quantitative measure of the degree of symmetry of the distribution. With major axis a , medium axis b and minor axis c , ie. $c < b < a$, the two axis ratios b/a and c/a are given by

$$\frac{b}{a} = \sqrt{\frac{a_2}{a_1}}, \quad \frac{c}{a} = \sqrt{\frac{a_3}{a_1}}, \quad (38)$$

where $a_1 > a_2 > a_3$.

The object is almost spherical if both ratios b/a and c/a are close to one. Oblate objects have axis ratios $c \ll b \sim a$, prolate objects $c \sim b \ll a$.

5.2 Shape evolution

The top panel of fig. 7 shows the distribution of axis ratios of bound groups at the present epoch, the lower panel the same distribution at $a = 100$, by means of the 2-D distribution of the object axis ratios b/a and c/a . The probability distribution is shown by means of iso-probability greyscale values. The highest probability density have dark greyscale values, with gradually lowering probability density as the colour becomes lighter. Because $c < b < a$ objects only populate the righthand triangle of the diagram. Spherical groups are located at (1,1), oblate groups tend towards the line $b/a = 1$ while prolate groups are found near the diagonal $b/a = c/a$.

At $a = 1$ the mean value of the axis ratios is $(\langle b/a \rangle, \langle c/a \rangle) = (0.69, 0.48)$, with a standard deviation of $(\sigma_{b/a}, \sigma_{c/a}) = (0.13, 0.11)$. Lower values of c/a are hardly present, implying that there are hardly any thin pancake-shaped structures (in the sense of $c/a \rightarrow 0$). To some extent this may be a reflection of our bound group identification procedure, given its bias towards spherical configurations (see sect. 3.1.5). There are also almost no near-spherical objects. Given the relative youth of these supercluster objects this is hardly surprising, given the fact that the primordial density field does not contain spherical peaks (Bardeen et al. 1986). Overall, the spread of the object shape probability distribution is rather sizeable. Also we observe a slight tendency of the majority of groups to lie near the diagonal: *bound groups have a slight tendency to a prolate shape.*

In the far future, at $a = 100$, the situation for the supercluster complexes is radically different. The majority of objects are predominantly found to have a near-spherical shape. The mean values of the axis ratios for all bound

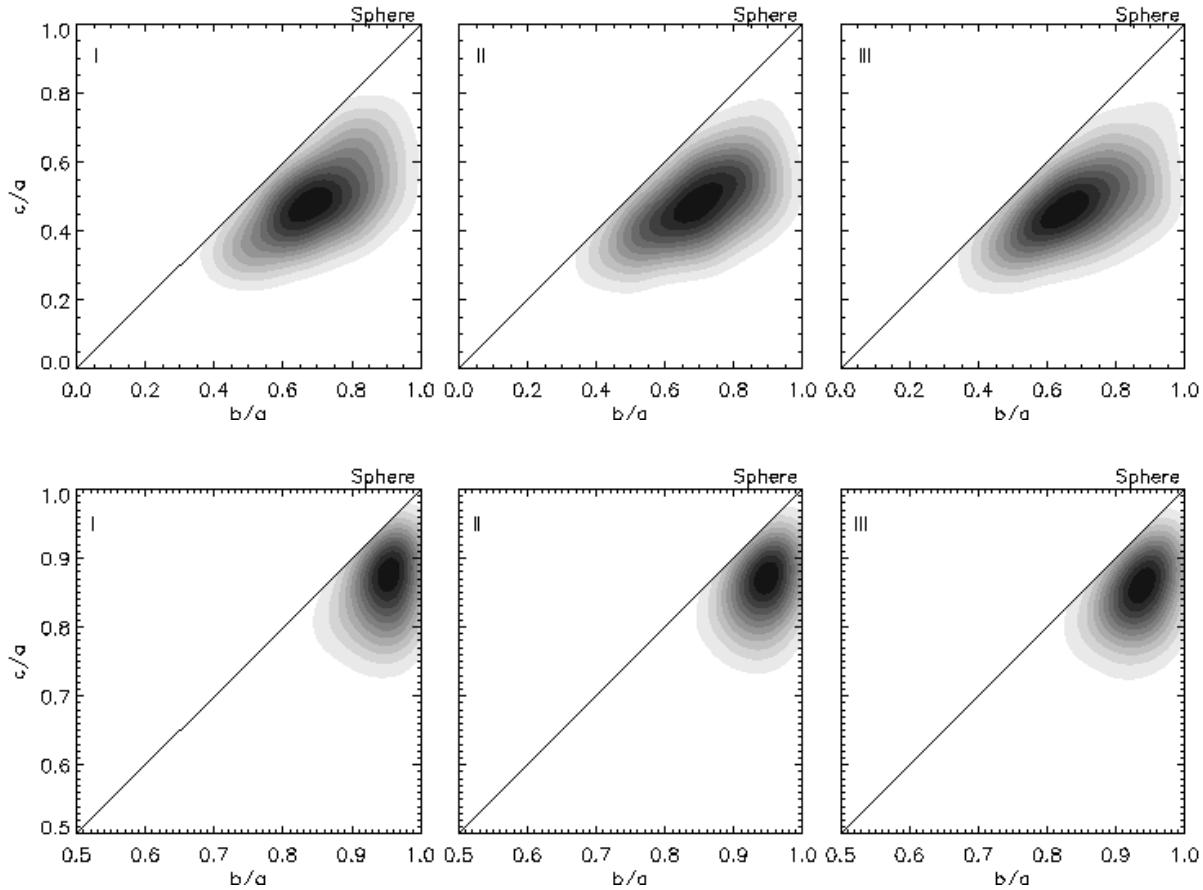


Figure 8. Distribution of axis ratios for three mass ranges. I: high-mass bound objects with $M > 4.8 \times 10^{14} h^{-1} M_{\odot}$. II: medium mass range bound objects, $2.8 \times 10^{14} h^{-1} M_{\odot} < M \leq 4.8 \times 10^{14} h^{-1} M_{\odot}$. III: low mass bound objects, $2 \times 10^{14} h^{-1} M_{\odot} < M \leq 2.8 \times 10^{14} h^{-1} M_{\odot}$. Each diagram shows the probability density distribution in the plane of b/a versus c/a values, with principal object axes $c < b < a$. Dark colors correspond to high probability, decreasing to lower probability as colours fade to light. Top row: axis ratio distribution at the current epoch, $a = 1$: prolate shapes are predominant in all three mass ranges. Bottom row: axis ratio distribution at $a = 100$: in all mass ranges there is a predominance for spherical shapes.

Table 1. Number of objects and average values of the axis ratios b/a and c/a , with their standard deviation, at $a = 1$ and $a = 100$ for three mass intervals I, II and III (with mass range set at $a = 1$).

			$\langle b/a \rangle$	$\langle c/a \rangle$	$\sigma_{b/a}$	$\sigma_{c/a}$
I	$M > 4.8 \times 10^{14} h^{-1} M_{\odot}$	$a = 1$	0.70	0.49	0.13	0.11
		$a = 100$	0.94	0.85	0.03	0.05
II	$2.8 \times 10^{14} h^{-1} M_{\odot} < M \leq 4.8 \times 10^{14} h^{-1} M_{\odot}$	$a = 1$	0.70	0.48	0.13	0.11
		$a = 100$	0.94	0.85	0.03	0.05
III	$2 \times 10^{14} h^{-1} M_{\odot} < M \leq 2.8 \times 10^{14} h^{-1} M_{\odot}$	$a = 1$	0.68	0.47	0.14	0.11
		$a = 100$	0.93	0.85	0.04	0.05

groups are $(\langle b/a \rangle, \langle c/a \rangle) = (0.94, 0.85)$, with rather small standard deviations $(\sigma_{b/a}, \sigma_{c/a}) = (0.03, 0.05)$.

The contrast between the shape distribution at $a = 1$ and at $a = 100$ is clear evidence of a significant and even radical internal evolution of the supercluster complexes. The change in shape of bound objects from a pronounced triaxial, nearly prolate, shape towards an almost spherical one is a

prominent manifestation of its ongoing dynamical evolution. The supercluster in fig. 3 represents a telling illustration of this change in shape. This strong development in shape takes place while there is virtually hardly any evolution on large scales.

5.3 Mass dependence

One potentially relevant issue concerns the possible dependence of shape on the mass of bound structures. In order to investigate this, we divide our sample in three mass ranges, all approximately including the same number of bound structures. Class I are the most massive third of objects, which at $a = 1$ have a mass $M > 4.8 \times 10^{14} h^{-1} M_{\odot}$. The medium mass class II includes objects with masses at $a = 1$ of $2.8 \times 10^{14} h^{-1} M_{\odot} < M \leq 4.8 \times 10^{14} h^{-1} M_{\odot}$ and the low mass class III are those with masses at $a = 1$ of $2 \times 10^{14} h^{-1} M_{\odot} < M \leq 2.8 \times 10^{14} h^{-1} M_{\odot}$.

We found that the three mass ranges have similar mean axis ratios, at the current epoch and at $a = 100$ (see Table 1). There is hardly any distinction between the shape distribution in the different mass ranges. This must be related to the fact that even though of different mass, the objects have been selected on the basis of similar (over)density values. The latter is an indication for the evolutionary state of the objects. In turn, as we have seen, this is reflected in their shape.

Figure 8 (top row) shows a contour map of the probability density distribution at $a = 1$ for the axis ratios for the three mass ranges described. We see a predominance for prolate shapes in every mass range. We also find that in all three mass ranges the superclusters, and other bound regions, assume a predominantly spherical morphology in the far future (Fig. 8, bottom row, also see Table 1).

With respect to their future evolution, we therefore may conclude that while bound objects grow in complete isolation and all substructure within their binding radius merges into one, single, virialized object they gradually attain a highly spherical shape.

5.3.1 Cluster vs. Supercluster Shapes

Keeping in mind that the objects in our sample are bound but perhaps not virialized, it is instructive to contrast them to virialized galaxy clusters. Although their masses may be comparable, the bound group radii are much larger as they have substantially lower densities than clusters. Within this larger region there is considerably more pronounced substructure.

The clusters in our simulation at $a = 1$ have a slight tendency towards prolateness, with average axis ratios $(\langle b/a \rangle, \langle c/a \rangle) = (0.83, 0.71)$ and standard deviation $(\sigma_{b/a}, \sigma_{c/a}) = (0.09, 0.09)$. These values are somewhat more pronounced than those quoted in other studies (e.g., Dubinski & Carlberg 1991; Katz 1991; van Haarlem & van de Weygaert 1993; Jing & Suto 2002; Kasun & Evrard 2005; Paz et al. 2006; Allgood et al. 2006). All agree that they tend to be more prolate as the halo mass increases. Dubinski & Carlberg (1991) found that halos are “strongly triaxial and very flat”, with mean axis ratios of $\langle b/a \rangle = 0.71$ and $\langle c/a \rangle = 0.50$. For simulations of isolated halos with different power spectra indices Katz (1991) found values ranging from $b/a \approx 0.84 - 0.93$ and $c/a \approx 0.43 - 0.71$, while for massive clusters Kasun & Evrard (2005) found peak values of $(b/a, c/a) = (0.76, 0.64)$.

Even though the radii of the bound structures in our sample are considerably larger than the virial radii of cluster, they do share the same tendency of having a prolate

shape. Given this, we do notice a distinct tendency of the superclusters to be more anisotropic than that of the virialized clusters. This is a reflection of their different dynamical state.

6 INTERNAL MASS DISTRIBUTION AND DENSITY PROFILES

We have seen that superclusters are gradually decoupling from the global cosmic expansion, and towards the far future evolve in isolation as genuine *cosmic islands*. As these contract and collapse, and finally even virialize, they will develop into a much more compact object. To understand their internal evolution it is important to look into the development of their internal mass distribution, and hence their density profile.

6.1 Supercluster Case Studies

Before trying to draw some general conclusions we look in more detail at the evolving mass distribution inside and around two representative individual superclusters in our sample. These are objects # 8 and # 98. The first one is a massive supercluster with a mass of $\sim 5.4 \times 10^{15} h^{-1} M_{\odot}$, while the second one has a mass of $\sim 3.6 \times 10^{15} h^{-1} M_{\odot}$. Supercluster # 8 is one of the most massive objects identified at $a = 1$ and also ends up as such at $a = 100$.

The evolution of the mass distribution in and around superclusters 8 and 98 from a weblike irregular and structured pattern at $a = 1$ into smooth and highly concentrated and nearly spherical mass clumps at $a = 100$ can be observed from the changing particle distributions in the lefthand and central frames of fig. 9. The top panels show the matter distribution of supercluster # 8 (lefthand: $a = 1$, centre: $a = 100$), the bottom panels that of supercluster # 98.

On all four panels we superimposed circles centered at the supercluster’s core. The solid circles are the “half-mass spheres” enclosing half of the total mass of the supercluster, while the dashed-dotted circles are the “virial spheres” with a radius equal to the virial radius and enclosing the central virialized core of the supercluster.

For the structure of the virial core we turn to the log-log diagrams of the radial density profiles $\rho(r)$, at both $a = 1$ (solid line) and $a = 100$ (dashed line), in fig. 10. All profiles have the same basic shape, a high density central core embedded within an isothermal power-law region with slope ~ -2 . While there may still be some deviations from this slope at $a = 1$, comparison with the inserted short line of slope -2 shows that at $a = 100$ the object cores are almost perfectly isothermal. The profiles confirm the impression from fig. 9 of the growth of the virial core, given the smooth near power-law profiles at $a = 100$ as opposed to the more irregular behaviour at the outer edges in the $a = 1$ profiles.

Along with the substantial rearrangement between $a = 1$ and $a = 100$ of their internal mass distribution into more compact and spherical mass concentrations, we note the radical change of the cosmic surroundings of both superclusters. At $a = 1$ both superclusters are still solidly integrated and embedded within the Megaparsec Cosmic Web. Their central cores, indicated by the “virial spheres”, are connected

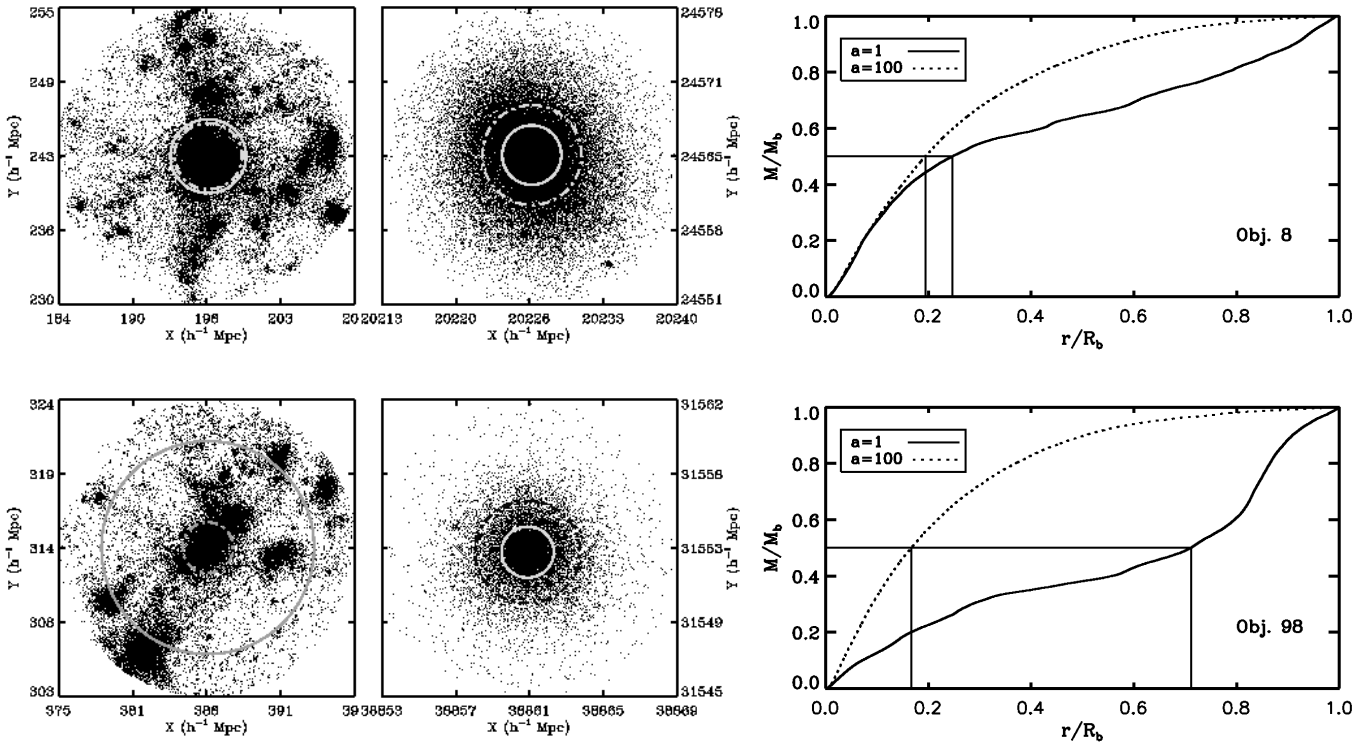


Figure 9. Top: supercluster # 8 ($M \sim 5.4 \times 10^{15} h^{-1} M_{\odot}$). Bottom: supercluster # 98 ($M \sim 3.6 \times 10^{15} h^{-1} M_{\odot}$). Dark matter/particle distribution at $a = 1$ (left) and $a = 100$ (centre) of object # 8, in physical coordinates. For comparison the half mass radius (solid circle) and the virial radius (dashed-dot circle) are superimposed on the matter distribution. Righthand panel: Cumulative mass distribution of the object as a function of its (normalized) radius r/r_b , at $a = 1$ (solid line) and at $a = 100$ (dotted line). The cumulative mass M/M_b is normalized with respect to the corresponding final (bound) mass M_b . The solid vertical lines indicate the value of the half-mass radius (for which $M/M_b=0.5$, the horizontal solid line), at both epochs $a = 1$ and $a = 100$.

to the surroundings via filamentary tentacles along which we find a large variety of mass clumps. Note that these outer structures at $a = 1$ are actually bound to the supercluster core and is bound to fall in and merge with the central cluster as time proceeds. At $a = 100$ the resulting supercluster concentrations have turned into isolated islands.

It is telling that at $a = 100$ both superclusters have attained an almost equivalent internal mass distribution, even though at $a = 1$ their morphology was quite different. At the present epoch, supercluster # 8 is already a centrally concentrated object. Given that the half-mass and virial spheres nearly overlap, we see that at $a = 1$ its virialized core contains nearly half of its total mass. This impression is underlined by the cumulative mass distribution. In the righthand panel we have plotted the cumulative mass $M_{sc}(r)$, in units of the total supercluster's mass M_b , as a function of radius r (in units of the supercluster's radius R_b). Comparison between the cumulative mass distribution at $a = 1$ (solid line) and $a = 100$ (dashed line) shows that there is only a small increase in mass in the inner region of the supercluster, immediately around the virialized core. Also the fact that the half-mass radius moves only slightly inward implies a mere moderate change in the inner mass distribution. It is the outer half of the supercluster's mass which rearranges itself more strongly: as it falls in towards the supercluster's interior the mass distribution becomes more concentrated and more regular.

The changing mass distribution is considerably more pronounced for supercluster # 98. At the current epoch its mass distribution is considerably more extended: its half-mass radius is located at an outward position. The central cluster core is not nearly as prominent as that in supercluster nr. 8. The supercluster's mass increases rather slowly until the half-mass radius. Beyond this radius there is an abrupt rise until the outer supercluster radius. This is related to the presence of another major mass clump near the outer boundary. When we would have observed this supercluster in the observational reality, we would find it to be dominated by two very rich clusters.

Also, we note that the superclusters do hardly gain mass from beyond their (bound) radius R_b . This we see reflected in the flattening of the cumulative mass curves at $a = 100$.

6.2 Supercluster Mass Concentration

From the discussion in the previous subsection we have learned that the superclusters are turning into bodies with a highly concentrated mass distribution at $a = 100$. It is only towards these later cosmic epochs that the superclusters have turned into highly nonlinear and concentrated regions. It would not be appropriate to seek to fit a theoretical density profile to their radial mass distribution in order to determine their concentration. Instead of seeking to fit an Einasto profile (Einasto 1965), or the profusely popular

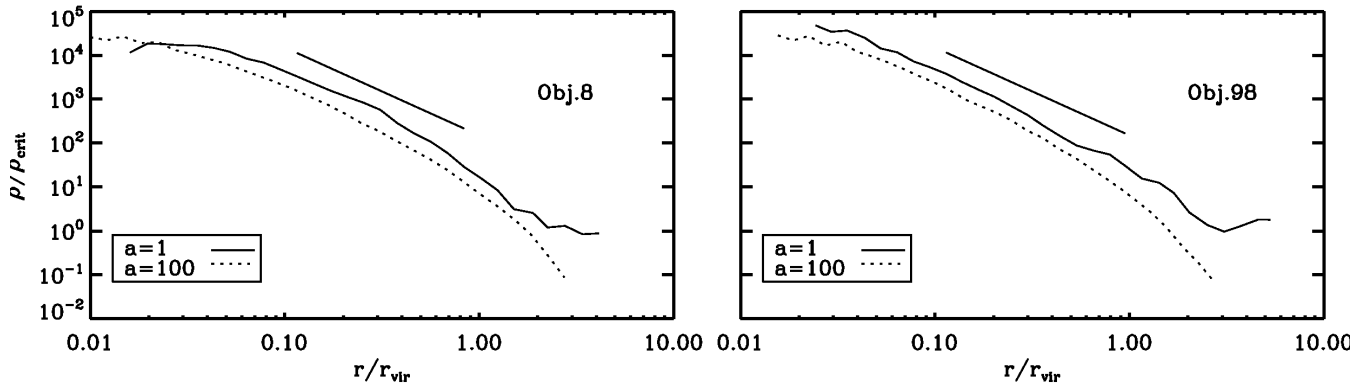


Figure 10. Radial density profiles of Object 8 (left panel) and Object 98 (right panel). In a log-log diagram each of the panels shows the radial density profile $\rho(r)$, in units of the critical density ρ_{crit} , as a function of the normalized radius r/r_{vir} (normalized wrt. the supercluster virial radius). Solid line: profile at $a = 1$. Dotted line: profile at $a = 100$. For comparison in both panels we include a short line with an isothermal slope -2 .

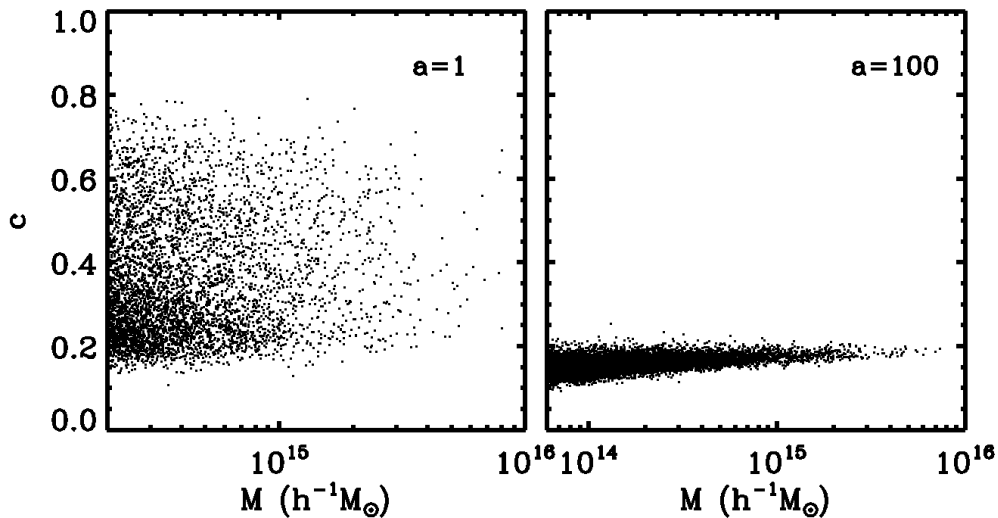


Figure 11. Concentration parameter c of each bound object in the bound object sample as a function of its mass M . The concentration parameter is the ratio of the half-mass radius of the object to its total binding radius r_b , $c \equiv r_{hm}/r_b$. Lefthand panel: $a = 1$. Righthand panel: $a = 100$. At $a = 100$ nearly all objects have a highly concentrated mass distribution, i.e. $c < 0.2$. Note that the bound object sample at $a = 1$ is complete down to $2 \times 10^{14} h^{-1} \text{Mpc}$, while at $a = 100$ it includes all objects down to $6 \times 10^{13} h^{-1} \text{Mpc}$.

universal NFW profile (Navarro, Frenk & White 1997), we therefore prefer to define a concentration parameter that is independent of assumptions about the dynamical state of the mass concentration,

$$c = \frac{r_{hm}}{r_b}, \quad (39)$$

where r_{hm} is the radius that encloses half of the mass. Note that with this definition a mass distribution with a “delta peak” in the centre would have $c = 0$, while a perfect uniform distribution would have $c \approx 0.8$. An isothermal distribution would correspond to $c = 0.5$.

Fig. 11 shows the distribution of c as a function of mass at $a = 1$ (left panel) and $a = 100$ (right panel). The panels do show the expected development. Over the whole mass range of bound objects at $a = 100$ we find them to be highly concentrated. Nearly all objects have $c < 0.2$, with an average concentration index $\bar{c} = 0.16$ and $\sigma_c = 0.02$. However, at the present epoch there still is a considerable spread of the concentration parameter ($\bar{c} = 0.35$, $\sigma_c = 0.14$). There are

even a few objects that get close to the $c = 0.8$ value corresponding to uniform mass profiles. Although there is a slight tendency towards higher concentrations, in general at $a = 1$ we find the concentration parameter to reflect the irregular and prominent outer mass distribution. This appears to be stronger in the case of the lower mass bound objects than for the $M > 10^{15} h^{-1} \text{M}_\odot$ superclusters.

7 SUPERCLUSTER SUBSTRUCTURE AND MULTIPLICITY FUNCTION

The third aspect of the internal evolution of superclusters is that of their substructure. Because superclusters are usually identified via their cluster content we focus on their *multiplicity* N_{SC} , i.e. the number of clusters they contain. Clusters are taken to be virialized subclumps with a mass higher than $3 \times 10^{13} h^{-1} \text{M}_\odot$, the low mass threshold virialized groups at $a = 1$. We should take into account that the definition of the

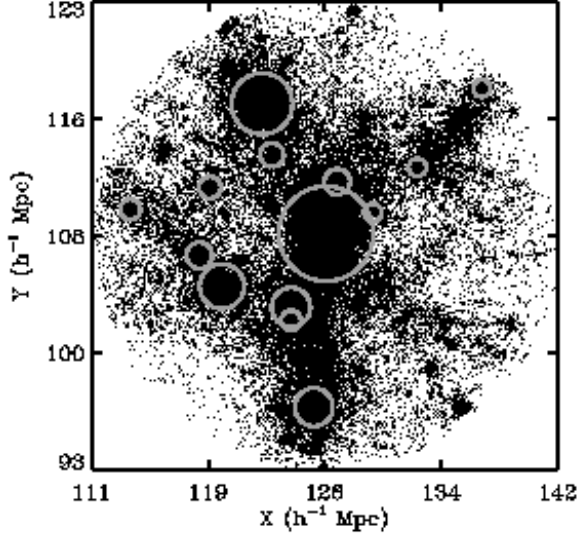


Figure 12. Supercluster multiplicity. The (dark) matter distribution within the binding radius of a supercluster, at $a = 1$. The clusters within the supercluster realm are indicated by circles. The size of the circle reflects the (virial) size of each cluster halo.

multiplicity N_{SC} does depend on the cluster mass threshold in our sample. While there is some arbitrariness in mass threshold, this will extend to the inferred supercluster multiplicity.

Fig. 12 gives an impression of the substructure of one of the superclusters in our sample, at $a = 1$. The cluster population within the supercluster is indicated by circles. The supercluster area is still a rather polymorphic assembly of matter, connected by means of filamentary extensions. The most prominent concentrations, the clusters, roughly follow these weblike structures.

Interestingly, we find that the mean mass of all the clusters in our simulation volume is $M_{cl} = 9.4 \times 10^{13} h^{-1} M_{\odot}$ while those residing within the realm of superclusters have an average mass $M_{cl} = 3.6 \times 10^{14} h^{-1} M_{\odot}$. The fact that superclusters contain more massive clusters may to some extent be the result of the active dynamical environment inside the supercluster. Because of the high concentration of subclumps, they are continuously merging and falling into ever more massive clumps. Clusters will be centres of action and thus grow rapidly in mass. Meanwhile, lower mass and lower density clumps are more liable to lose mass or even be gradually dismantled by the prevailing strong tidal forces in and near the superclusters. This may add to the bias towards higher cluster masses inside superclusters.

One of the principal findings of our study is that, without exception, at $a = 100$ all superclusters in our sample have attained a multiplicity one. By that time they all have evolved into compact and smooth density concentrations, akin to the one seen in fig. 3. The hierarchical development of the supercluster involves the gradual merging of its constituent subclumps into one condensed object. As a result we see superclusters containing several to dozens of clusters ultimately end up as an object of unit multiplicity.

Turning to the present epoch, we assess the multiplicity

function for the 17 most massive superclusters, those whose mass is in excess of $M = 5 \times 10^{15} h^{-1} M_{\odot}$. When evaluating the (cumulative) multiplicity distribution, the number density of superclusters with more than N_{SC} clusters (fig. 13, left-hand), we see that half of the superclusters have 10 or more members. Also we find that larger and more massive superclusters do have a higher number of cluster members. This trend is particularly strong for superclusters with $N_{SC} < 10$, but for an not entirely understood reason seems to level off for more massive and larger supercluster complexes. This is clearly shown in the central panel of fig. 13, plotting the multiplicity N_{SC} against supercluster radius M_{SC} .

Because we have used a physical criterion for the identification of clusters and superclusters, we assume the inferred multiplicities to be close to the natural one. Usually supercluster multiplicity estimates do depend to some extent on the supercluster identification procedure. There is certainly a dependence on percolation radius when identified on the basis of a percolation criterion (Zeldovich et al. 1982; Shandarin & Zeldovich 1989).

This may be one of the reasons why our measured supercluster multiplicities do seem to differ from those obtained in other studies (in addition to the dependence on cluster mass threshold). For example, Wray et al. (2006) did find superclusters with more than 30 members. This certainly relates to the choice of linking length for defining the supercluster: dependent on the linking length they found maximum supercluster sizes ranging from $\sim 30 h^{-1} \text{Mpc}$ to $\sim 150 h^{-1} \text{Mpc}$. The latter are much larger than the superclusters we find according to our density-based definition.

8 SHAPLEY-LIKE SUPERCLUSTERS

The Shapley concentration, first noted by Shapley (1930), is one of most outstanding supercluster complexes out to $z = 0.12$ (see Raychaudhury 1989; Ettori 1997; Quintana et al. 2000; Proust et al. 2006). It amasses at least 30 rich Abell galaxy clusters in a core region of $\sim 25 h^{-1} \text{Mpc}$ and is located at a distance of $\sim 140 h^{-1} \text{Mpc}$. Its total mass is estimated to be $\sim 5 \times 10^{16} h^{-1} M_{\odot}$ within a radius of $\sim 30 h^{-1} \text{Mpc}$ (see e.g. Proust et al. 2006). Almost as massive is another similar assembly of massive clusters in the local Universe, the Horologium-Reticulum supercluster. Both may have a major influence on the motion of the Local Group with respect to the background Universe (see e.g. Plionis & Valdarnini 1991; Kocevski & Ebeling 2006).

We investigated in how far we can find back the equivalents of the Shapley and Horologium superclusters in our simulation. On the basis of the mass functions determined in sect. 4.2 we estimate that the most massive supercluster present in a volume akin to the local Universe ($z < 0.1$) may have a mass of $\sim 8 \times 10^{15} h^{-1} M_{\odot}$. This mass is slightly larger than the one in the bound region of the Shapley concentration as determined by Dünner et al. (2008). Extrapolating this conclusion, we find that one may typically find two Shapley-like superclusters out to $z \approx 0.1$, a volume of the size of the Local Universe.

When turning towards the multiplicity of the detected simulation superclusters, we find from Fig. 13 that the largest supercluster in the Local Universe would have 15 members. A Shapley-like supercluster would have a radius

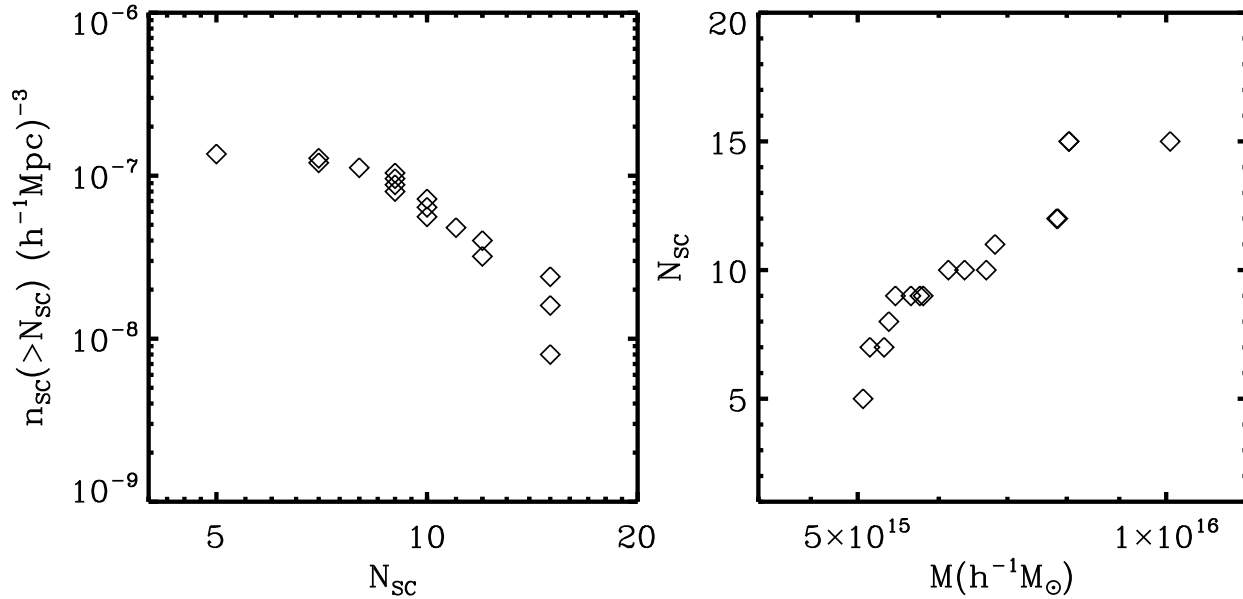


Figure 13. Supercluster multiplicity. Left panel: the cumulative multiplicity distribution $n_{sc}(N_{sc})$ of superclusters containing N_{sc} or more clusters, at the present epoch $a = 1$. The distribution concerns the 17 most massive superclusters in the simulation, with $M > 10^{15} h^{-1} M_{\odot}$. Righthand: Supercluster multiplicity N_{sc} as a function of the mass M of the supercluster.

of $\sim 14h^{-1}\text{Mpc}$ and host between 10 to 15 members, close to the number found in the bound region of the Shapley supercluster (Dünner et al. 2008), which contains $\sim 1/3$ of the clusters traditionally assigned to this structure (e.g. Proust et al. 2006). In the observational reality of our Local Universe ($z < 0.1$), we find 5 superclusters with 10 or more members, the largest one containing 12 members (see e.g. Einasto et al. 1994).

9 CONCLUSIONS

In this work, we studied several properties of bound structures, such as their mass function, shape and density profile. These bound structures were defined by the density criterion derived in Paper I (see eqn. 17), and identified from a $500h^{-1}\text{Mpc}$ cosmological box with 512^3 dark matter particles in a ΛCDM ($\Omega_{m,0} = 0.3$, $\Omega_{\Lambda,0} = 0.7$ and $h = 0.7$) Universe. We ran the simulation up to $a = 100$, which is a time where structures have stopped forming. We use HOP in order to identify independently virialized structures, both at $a = 1$ and $a = 100$. Our main results can be summarized as follows:

- The marginally bound objects that we study resemble the superclusters in the observed Universe. While clusters of galaxies are the most massive, fully collapsed and virialized objects in the Universe, superclusters are the largest bound –but not yet collapsed– structures in the Universe.
- The superclusters are true *island Universes*: as a result of the accelerating expansion of the Universe, no other, more massive and larger, structures will be able to form.
- While the superclusters collapse between $a = 1$ and $a = 100$, their surroundings radically change. At the present epoch solidly embedded within the Cosmic Web, at $a = 100$ they have turned into isolated cosmic islands.

- The mass functions in the simulations are generally in good agreement with the theoretical predictions of the Press-Schechter, Sheth-Tormen, and Jenkins mass functions. At $a = 1$, the Sheth-Tormen prescription provides a better fit. At $a = 100$, the pure Press-Schechter function seems to be marginally better. This may tie in with the more anisotropic shape of superclusters at $a = 1$ in comparison to their peers at $a = 100$.

- While the large-scale evolution of superclusters comes to a halt as a result of the cosmic acceleration, their internal evolution continues until they have evolved into a single virialized clump, sometimes up to $a = 100$.

- As a result of their collapse, the shape of the bound objects appears to change from prolate at $a = 1$ into almost spherical at $a = 100$. We find that at $a = 1$ their mean axis ratios are $(\langle b/a \rangle, \langle c/a \rangle) = (0.69, 0.48)$. At $a = 100$, they have mean axis ratios of $(\langle b/a \rangle, \langle c/a \rangle) = (0.94, 0.85)$.

- The change in the internal mass distribution and that in the surroundings is directly reflected by the radial density profile. The inner density profile steepens substantially when the inner region of the supercluster is also still contracting. On the other hand, when at $a = 1$ it has already developed a substantial virialized core, the inner density profile hardly changes.

- The mass profile in the outer realms of the supercluster always changes radically from $a = 1$ to $a = 100$. At $a = 1$ it shows an irregular increase as a function of radius, reflecting the surrounding inhomogeneous mass distribution of the Cosmic Web. By $a = 100$ the superclusters have developed a smooth, regular and steadily increasing mass profile.

- At the current epoch the superclusters still contain a substantial amount of substructure. Particularly interesting is the amount of cluster mass objects within its realm, expressed in the so called *multiplicity function*. Restricting ourselves to superclusters with a mass larger than $5 \times 10^{15} h^{-1} M_{\odot}$, of which we have 17 in our simulation sam-

ple, we find a multiplicity of 5 to 15 at the current epoch. By contrast, all these have evolved into concentrated singular mass clumps of unit multiplicity.

• In a region of a volume comparable to the Local Universe ($z < 0.1$) we find that the most massive supercluster would have a mass of $\sim 8 \times 10^{15} h^{-1} M_{\odot}$. This is slightly more massive than the mass of the Shapley Supercluster given in Dünner et al. (2008). When turning towards the multiplicity, we find that the largest superclusters in the Local Universe would host between 10 to 15 members, close to the number found in the bound region of the Shapley supercluster (Dünner et al. 2008) (which according to Proust et al. (2006) contains $\sim 1/3$ of the clusters traditionally assigned to this structure).

ACKNOWLEDGMENTS

PA and RvdW are grateful to Bernard Jones for valuable and incisive comments and many useful discussions and Thijs van der Hulst for continuous and unceasing encouragement. HQ is grateful to the FONDAP Centro de Astrofísica for partial support, AR acknowledges support by FONDECYT Regular Grant 1060644 and in addition AR and HQ thank Proyecto Basal PFB-06/2007. AM was supported by the Fondo Gemini-Conicyt through grant no. 32070013. PA acknowledges support by a NOVA visitor grant during the completion phase of the manuscript.

REFERENCES

- Allgood B., Flores R. A., Primack J. R., et al., 2006, MNRAS, 367, 1781
 Bahcall N.A., 1988, ARAA, 26, 631
 Bardeen J. M., Bond J. R., Kaiser N., Szalay A. S., 1986, ApJ, 304, 15
 Basilakos S., Plionis M., Rowan-Robinson M., 2001, MNRAS, 323, 47
 Basilakos S., Plionis M., Yepes G., Gottlöber S., Turchaninov V., 2006, MNRAS, 365, 539
 Bond J. R., Cole S., Efstathiou G., Kaiser N., 1991, ApJ, 379, 440
 Bond J.R., Myers S.T., 1996, ApJS, 103, 1
 Bryan G. L., Norman M. L., 1998, ApJ, 495, 80
 Busha M. T., Adams F. C., Wechsler R. H., Evrard A. E., 2003, ApJ, 596, 713
 Busha M. T., Evrard A. E., Adams F. C., 2007, ApJ, 665, 1
 Carroll S. M., Press W. H., Turner E. L., 1992, ARA&A, 30, 499
 Chiueh T., He X.-G., 2002, Phys. Rev. D, 65, 123518
 Cohn J. D., Bagla J. S., White M., 2001, MNRAS, 325, 1053
 Desjacques V., 2008, MNRAS, in press
 Dubinski J., Carlberg R. G. 1991, ApJ, 378, 496
 Dünner R., Araya P. A., Meza A., Reisenegger A., 2006, MNRAS, 366, 803: Paper I
 Dünner R., Reisenegger A., Meza A., Araya P. A., Quintana H. 2007, MNRAS, 376, 1577
 Dünner R., Reisenegger A., Meza A., et al., 2008, in preparation
 Efstathiou G., Frenk C. S., White S. D. M., Davis M., 1988, MNRAS, 235, 715
 Einasto J., 1965, Trudy Inst. Astrofiz. Alma-Ata, 5, 87
 Einasto M., Einasto J., Tago E., Dalton G.B., Andernach H., 1994, MNRAS, 269, 301
 Einasto M., Saar E., Tago E., Müller V., Andernach H., ApJ, 122, 2222
 Einasto M., Saar E., Liivamägi L. J., et al., 2007, A&A, 476, 697
 Eisenstein D.J., Loeb A., 1995, ApJ, 439, 520
 Eisenstein D. J., Hut P., 1998, ApJ, 498, 137
 Eke V.R., Cole S., Frenk C.S., 1996, MNRAS, 282, 263
 Ettori S., Fabian A.C., White D.A., 1997, MNRAS, 289, 787
 Evrard A. E., MacFarland T. J., Couchman H. M. P., et al., 2002, ApJ, 573, 7
 Governato F., Babul A., Quinn T., et al., 1999, MNRAS, 307, 949
 Gunn J. E., Gott J. R. I., 1972, ApJ, 176, 1
 Giovanelli R., Haynes M.P., Chincarini G.L., 1986, ApJ, 300, 77
 Heath D. J. 1977, MNRAS, 179, 351
 Hoffman Y., Lahav O., Yepes G., Dover Y. 2007, JCAP, 10, 16
 Icke V., 1973, A&A, 27, 1
 Jenkins A., Frenk C. S., White S. D. M., et al., 2001, MNRAS, 321, 372
 Jing Y. P., Suto Y., 2002, ApJ, 574, 538
 Kasun S. F., Evrard A. E., 2005, ApJ, 629, 781
 Katz N., 1991, ApJ, 368, 325
 Kitayama T., Suto Y., 1996, ApJ, 469, 480
 Kocevski D.D., Ebeling H., 2006, ApJ, 645, 1043
 Lacey C., Cole S., 1993, MNRAS, 262, 627
 Lacey C. Cole S., 1994, MNRAS, 271, 676
 Lahav O., Lilje P. B. Primack J. R., Rees M. J., 1991, MNRAS, 251, 128
 Landau L.D., Lifschitz E.M., 1960, Mechanics, Pergamon Press, Oxford
 Lilje P. B., Lahav O., 1991, ApJ, 374, 29
 Lynden-Bell D., 1964, ApJ, 139, 1195
 Nagamine, K., & Loeb, A. 2003, New Astronomy, 8, 439
 Navarro J. F., Frenk C. S., White S. D. M., 1997, ApJ, 490, 493
 Oort J.H., 1983, ARAA, 21, 373
 Paz, D. J., Lambas, D. G., Padilla, N., & Merchán, M. 2006, MNRAS, 366, 1503
 Peacock J.A., Heavens A.F., 1985, MNRAS, 217, 805
 Peacock J.A., Heavens A.F., 1990, MNRAS, 243, 133
 Peebles, P. J. E. 1980, The large-scale structure of the universe (Research supported by the National Science Foundation. Princeton, N.J., Princeton University Press, 1980, p. 435)
 Peebles, P. J. E. 1984, ApJ, 284, 439
 Plionis M., Valdarnini R., 1991, MNRAS, 249, 46
 Plionis, M., Valdarnini, R., & Jing, Y.-P. 1992, ApJ, 398, 12
 Press, W. H. & Schechter, P. 1974, ApJ, 187, 425
 Proust D., Quintana H., Carrasco E.R., Reisenegger A., Slezak E., Muriel H., Dünner R., Sodr  L. Jr., Drinkwater M.J., Parker Q.A., Ragone C.J., 2006, A&A, 447, 133
 Quintana, H., Carrasco, E. R., & Reisenegger, A. 2000, AJ, 120, 511

Raychaudhury S., 1989, *Nature*, 342, 251
 Sathyaprakash B.S., Sahni V., Shandarin S.F., 1996, *ApJ*, 462, 5
 Sathyaprakash B.S., Sahni V., Shandarin S.F., 1998, *ApJ*, 508, 551
 Shandarin S.F., Zeldovich Ya.B., 1989, *Rev.Mod.Phys.*, 61, 185
 Shandarin S.F., Sheth J.V., Sahni V., 2004, *MNRAS*, 353, 162
 Shapley H., Ames A., 1930, *Harvard Coll. Obs. Bull.*, 880, 1
 Sheth R. K., 1998, *MNRAS*, 300, 1057
 Sheth R. K., Tormen G. 1999, *MNRAS*, 308, 119
 Sheth J.V., Sahni V., Shandarin S.F., Sathyaprakash B.S., 2003, *MNRAS*, 343, 22
 Spergel D. N., Verde L., Peiris H. V., et al., 2003, *ApJS*, 148, 175
 Springel V., 2005, *MNRAS*, 364, 1105
 van de Weygaert R., Bond J.R., 2008, in *A Pan-Chromatic View of Clusters of Galaxies and the Large-Scale Structure*, ed. M. Plionis, O. Lopez-Cruz, D. Hughes, *Lect. Notes Phys.*, 740, 335 (Springer)
 van Haarlem M., van de Weygaert R., 1993, *ApJ*, 418, 544
 White S.D.M., Silk J., 1979, *ApJ*, 231, 1
 Wray J. J., Bahcall N. A., Bode P., Boettiger C., Hopkins P. F., 2006, *ApJ*, 652, 907
 Zeldovich Ya.B., 1970, *A&A*, 5, 84
 Zeldovich Ya.B., Einasto J., Shandarin S.F., 1982, *Nature*, 300

APPENDIX A: PRESS-SCHECHTER MODELLING OF SUPERCLUSTERS

According to the Press-Schechter formalism (Press & Schechter 1974; Peacock & Heavens 1990; Bond et al. 1991; Sheth 1998), the comoving number density of halos of mass M at redshift z , in a cosmic background of density ρ_u , is given by the expression

$$\frac{dn}{dM} = 2 \frac{\rho_u}{M} \left| \frac{\partial F}{\partial M} \right| = \sqrt{\frac{2}{\pi}} \frac{\rho_u}{M^2} \frac{\delta_c}{\sigma(M, z)} \left| \frac{d \ln \sigma(M, z)}{d \ln M} \right| e^{-\frac{\delta_c^2}{2\sigma^2(M, z)}}. \quad (\text{A1})$$

in which δ_c/σ quantifies the relative critical overdensity δ_c of collapse with respect to the variance of density fluctuations $\sigma(M, z)$ on a mass scale M . For a scenario with a power spectrum $P(k)$ of the linear density field,

$$\sigma^2(M) = 4\pi \int_0^\infty P(k) \omega(kr) k^2 dk, \quad (\text{A2})$$

where $\omega(kr)$ is the Fourier space representation of a real-space top-hat filter enclosing a mass M in a radius r at the mean density of the Universe, which is given by

$$\omega(kr) = 3 \left[\frac{\sin(kr)}{(kr)^3} - \frac{\cos(kr)}{(kr)^2} \right]. \quad (\text{A3})$$

The critical spherical collapse overdensity value δ_c has a weak dependence on the cosmological background (Gunn & Gott 1972; Lacey & Cole 1993; Eke et al. 1996; Kitayama & Suto 1996). Useful fitting formulae for the linear spherical model collapse value δ_c were obtained by

Navarro, Frenk & White (1997) for $\Omega_\Lambda = 0$ FRW universes and for flat Universes,

$$\delta_c(\Omega_m) = \begin{cases} 0.15(12\pi)^{2/3} \Omega_m^{0.0185} & \Omega_m < 1, \Omega_\Lambda = 0, \\ 0.15(12\pi)^{2/3} \Omega_m^{0.0055} & \Omega_m + \Omega_\Lambda = 1. \end{cases} \quad (\text{A4})$$

A similar expression for the critical linear virial density has been given by Bryan & Norman (1998),

$$\Delta_{vir} = \begin{cases} 18\pi^2 + 82(\Omega_m - 1) - 39(\Omega_m - 1)^2 & \Omega_m + \Omega_\Lambda = 1 \\ 18\pi^2 + 60(\Omega_m - 1) - 32(\Omega_m - 1)^2 & \Omega_m < 1, \Omega_\Lambda = 0 \end{cases} \quad (\text{A5})$$

While most applications of the (extended) PS formalism assume perfectly spherical collapse, we know that generic gravitational collapse of primordial density peaks proceeds anisotropically. Sheth & Tormen (1999) improved the PS formalism by taking into account the anisotropic collapse implied by the anisotropic primordial shape of density peaks and the anisotropic tidal stresses imparted by external mass concentrations. Modelling this by means of the ellipsoidal collapse model (e.g., Lynden-Bell 1964; Icke 1973; White & Silk 1979; Eisenstein & Loeb 1995; Bond & Myers 1996; Desjacques 2008) they showed this translates into a more fuzzy *moving collapse density barrier*. The resulting mass function,

$$\frac{dn_{ST}}{dM} = A \sqrt{\frac{2a}{\pi}} \left[1 + \left(\frac{\sigma(M)^2}{a\delta_c^2} \right)^p \right] \frac{\rho_u}{M^2} \frac{\delta_c}{\sigma(M)} \left| \frac{d \ln \sigma(M)}{d \ln M} \right| e^{-\frac{a\delta_c^2}{2\sigma^2(M)}}, \quad (\text{A6})$$

with $a = 0.707$, $p = 0.3$ and $A \approx 0.322$, gives a substantially better fit to the mass functions obtained in N-body simulations. In comparison with the standard PS mass function, ST predicts a higher abundance of massive objects and a smaller number of less massive ones. Later, Jenkins et al. (2001) reported a small disagreement with respect to N-body simulations: underpredictions for the massive halos and overpredictions for the less massive halos. They suggested the alternative expression:

$$\frac{dn_J}{dM} = A \frac{\rho_u}{M^2} \frac{d \ln \sigma(M)}{d \ln M} e^{(-\ln \sigma^{-1} + B)\epsilon}. \quad (\text{A7})$$

with $A = 0.315$, $B = 0.61$ and $\epsilon = 3.8$. Note, however, that their expression does not depend explicitly on δ_c . They showed that “for a range of CDM cosmologies and for a suitable halo definition, the simulated mass function is almost independent of epoch, of cosmological parameters, and of initial power spectrum”.

This paper has been typeset from a \TeX / \LaTeX file prepared by the author.